Environmental Rock-Magnetism of Cenozoic Red Clay in the South Pacific Gyre

A Dissertation Submitted to
the Graduate School of Life and Environmental Sciences,
the University of Tsukuba
in Partial Fulfillment of the Requirements
for the Degree of Doctor of Philosophy in Science
(Doctorial Program in Earth Evolution Sciences)

Takaya SHIMONO

Contents

Abstract……..…….....i

List of figures…….……..……...v

1. Introduction……1

2. Geological setting and materials.....……4

3. Methods

3.1.Magnetostratigraphy.....5

Onboard paleomagnetic measurements

Post-cruise sampling and measurements

3.2. Environmental rock-magnetism.....7

S ratio and k_{ARM}/SIRM

FORC diagram

IRM component analysis

Low-temperature magnetic measurement

High-temperature magnetic measurement

Observation with transmission electron microscope (TEM)

3.3. Rare-earth element content……12

4. Results

4.1. Age model……...12

Magnetostratigraphy

Age estimation from DSDP Site 596

4.2. Environmental rock-magnetism……..15

FORC diagram

k_{ARM}/SIRM ratio

IRM component analysis

S ratio

Low-temperature magnetic measurement

High-temperature magnetic measurement

Observation with transition electron microscope (TEM)

5. Discussion……19

Biogenic magnetite in red clay

Cenozoic environmental change

Possible relation of magnetic properties and ΣREY contents

6. Conclusions……24

7. Acknowledgements……25

8. References……26

Figure captions……37

Abstract

Red clay occupies approximately 40 % of the global ocean floor. Paleoceanographic and paleomagnetic studies of red clay were limited so far because red clay does not yield microfossils that can be used for precise age estimation and sedimentation rates were extremely low. However, red clay could be useful for elucidating long-range environmental changes. Recently, red clay has attracted interest because of the discovery that red clay rich in ΣREY (rare-earth elements and yttrium) distributes widely in the Pacific Ocean. I conducted an environmental rock-magnetic study using the Integrated Ocean Drilling Program (IODP) Site U1365 cores (75.5 m long above ~125 Ma basement) taken at the western edge of the South Pacific Gyre in order to investigate long-range climatic and paleoceanographic changes during the Cenozoic. This is the first environmental rock-magnetic study in the South Pacific Gyre ever. I also investigate a relation between magnetic properties and ΣREY contents of the red clay.

Magnetostratigraphy could be established above about 6 meters below the seafloor (mbsf) (about 5 Ma). Below about 6 mbsf, the ages of the Site U1365 cores were transferred from published ages of nearby Deep Sea Drilling Project (DSDP) Site 596, which is based mainly on a constant Cobalt flux model, by inter-core correlation using magnetic susceptibility and ΣREY variation patterns. On first-order reversal curve diagrams, a non-interacting single-domain magnetic component, which is a characteristic of biogenic magnetite, was recognized throughout the sediment column. The ratio of anhysteretic remanent magnetization (ARM) susceptibility to saturation isothermal remanent magnetization (IRM) (k_{ARM} /SIRM), a proxy of the biogenic to terrigenous magnetic components, is high, in particular below about 8.0 mbsf (about 35 Ma). Biogenic magnetite was further identified on the transmission electron

microscopy. These line of evidence shows that biogenic magnetite dominates magnetic mineral assemblages in red clay, which does not have the oxic-anoxic transition zone (OATZ) down to the basement. This results conflict with the current thoughts that magnetotactic bacteria live in a strong vertical chemical gradient near the OATZ. In the results of IRM component analyses, the middle-coercivity component likely carried by maghemite increased since about 35 Ma, whereas S ratios and k_{ARM}/SIRM values decreased. The increase accelerated after 5 Ma. These observations suggest increases of the input of terrigenous magnetic minerals, which is inferred to be transported as eolian dust. The Eocene/Oligocene boundary (about 34 Ma) is known as the time of a major global cooling, and the increase of eolian dust supply in the South Pacific may have occurred since then. Northward shift of Australia to an arid region in middle latitudes should have also contributed to the increase of eolian dust supply. The second increase of eolian dust flux at about 5 Ma may have been caused by a further growth of the Antarctic glaciation at about 6 Ma. I also discuss a possible relationship between ΣREY content and magnetic properties. A ΣREY content peak occurred close to the sharp upward decrease in the k_{ARM}/SIRM ratio at about 35 Ma. An interval of high magnetic susceptibility occurs above the peak of ΣREY contents. These characteristics were also observed in red clay cores near Minami-Torishima in the northwest Pacific. This suggests that the enhanced ΣREY concentration may have occurred in association with a common paleoceanographic event near the Eocene-Oligocene boundary.

Key words

red clay, environmental rock-magnetism, South Pacific Gyre, biogenic magnetite, eolian dust, rare-earth content, Cenozoic

List of Figures

Figure 1-1. Distribution of various lithologies of deep-sea sediments…….42

Figure 2-1. Location of IODP Site U1365……43

Figure 2-2. Surface chlorophyll-*a* concentrations in the Pacific……..44

Figure 2-3. Paleopositions of Site U1365 since 100 Ma……..45

Figure 2-4. Lithologic summary and estimated ages of Site U1365……46

Figure 2-5. Dissolved oxygen concentration of interstitial water at Site U1365……..47

Figure 4-1. Age model based on magnetostratigraphy…….48

Figure 4-2. Stepwise alternating and thermal demagnetization diagrams of samples with stable remanent magnetization……49

Figure 4-3. Sedimentation rate based on magnetostratigraphy above about 6 mbsf (about 5 Ma)……50

Figure 4-4. Examples of unstable remanent magnetization……..51

Figure 4-5. Comparison of inclinations from onboard and post-cruise measurements……52

Figure 4-6. Variations of magnetic susceptibility with depth……53

Figure 4-7. Inter-core correlations between IODP Site U1365 and DSDP Site 595 using magnetic susceptibility and ΣREY content variation patterns……..54

Figure 4-8. Agreement of susceptibility and ΣREY content variation patterns after inter-core correlation…….55

Figures 4-9. Examples of high-resolution first-order reversal curve (FORC) diagrams and coercivity profiles……..56

Figure 4-10. An example of low-resolution FORC diagram…….59

Figure 4-11. Variations of k_{ARM}/SIRM ratio with depth……...60

Figure 4-12. Examples of FORC diagrams and results of isothermal remanent magnetization component analyses……...61

Figure 4-13. Variations of S ratios, $S_{-0.1T}$ and $S_{-0.3T}$, with depth……62

Figures 4-14. Examples of low-temperature magnetic measurements……..63

Figure 4-15. Examples of thermo-magnetic curves……...65

Figures 4-16. Transmission electron microscope (TEM) images of magnetic extracts……66

Figure 5-1. Summary of magnetic property changes with age……..68

Figure 5-2. Summary of temporal variations in rock-magnetic properties, ΣREY content, and sedimentation rates……69

Fig. 5-3. Paleopositions of Australia and Site U1365 since 55 Ma in relation to an arid zone….70

Fig. 5-4. Variations of magnetic susceptibility, k_{ARM}/SIRM ratio, and ΣREY content with depth for a red clay core taken near Minami-Torishima……71

1. Introduction

Unfossiliferous pelagic sediments with brownish color are called red clay. Red clay accumulates on the sea floor far from the land below the carbonate compensation depth (CCD) except for high ocean productivity provinces along the equator and high latitudes (Brown et al., 1989) (Figure 1-1). Sedimentation rates of red clay are extremely low, less than a few millimeters per thousand years. Red clay provinces in the middle latitudes occupy about 40 % of the global ocean floor. In the Pacific Ocean, the North Pacific Gyre (NPG) and the South Pacific Gyre (SPG) are the two major red clay provinces.

Paleoceanographic studies of red clay were limited so far, because red clay does not yield microfossils that can be used for precise age estimation, and because age resolution is quite low due to the extremely slow sedimentation. However, red clay could be useful for estimating long-range paleoceanographic changes. Sedimentological studies revealed that the major source of red clay in the North Pacific is eolian dust transported from arid regions of the Asian continent (Rex and Goldberg, 1958; Blank et al., 1985). Eolian dust flux and grain size increased in the Quaternary associated with the northern hemisphere glaciation (Janecek and Rea, 1983, Janecek, 1985). A long-range Cenozoic sedimentation history of the central North Pacific was studied using a 24.3 m-long red clay core (LL44-GPC3) (Kyte et al., 1992; Pettke et al., 2002). As for paleomagnetism, it has been known that magnetostratigraphy can be established back to only about 3 Ma in red clay in the North Pacific, and natural remanent magnetization is often unstable for older ages (Kent and Lowrie, 1974; Yamazaki and Ioka, 1997).

Recently, red clay has attracted interest since Kato et al. (2011) reported that red clay rich in ΣREY (rare-earth element and yttrium) distributes widely in the Pacific Ocean. The red clay

provinces roughly coincide with the areas of high-REY contents. Among the cores studied by Kato et al. (2011), particulaly REY-rich red clay (2110 ppm at the maximum) of about 40 m thick occurs below 13.5 meters below the seafloor (mbsf) at the Deep Sea Drilling Project (DSDP) Site 596 at the western edge of the SPG.

Rock magnetic techniques can be used to investigate the formation, transportation, deposition, and post-depositional alteration of magnetic minerals under various environmental processes (Thompson and Oldfield, 1986; Verosub and Roberts, 1995; Evans and Heller, 2003). Rock-magnetic applications to environmental problems are called environmental magnetism. This has become widely used to paleoceanographic and paleoclimatic studies with the recent progress in rock-magnetic techniques (e.g., Doh et al., 1988; Bareille et al. 1994; Yamazaki and Ioka, 1997; Schmieder et al. 2000; Watkins et al., 2007; Suganuma et al., 2009, Roberts et al., 2011; Yamazaki, 2012; Yamazaki and Ikehara, 2012). As sediments more or less contain iron-bearing minerals, environmental magnetism can be applied widely. As for environmental magnetic studies of red clay, Yamazaki and Ioka (1997) indicated that terrigenous magnetic minerals such as hematite increased since about 3 Ma in the NPG. Doh et al. (1988) presented long-term variations of magnetic grain size in the NPG during the Cenozoic. They interpreted the magnetic grain-size change in terms of paleoclimate such as the intensity of atmospheric circulation.

Recently, the importance of biogenic magnetite, which is produced by magnetotactic bacteria, has been recognized as an origin of magnetic minerals in marine sediments (Yamazaki, 2009; Roberts et al., 2012; Yamazaki and Ikehara, 2012). Magnetotactic bacteria produce chains of intracellular magnetite and/or greigite crystals (magnetosomes), and respond to an ambient magnetic field (Blakemore, 1975, 1982; Mann et al., 1990). After death of magnetotactic bacteria,

the magnetosomes remain in sediments as fossils (Kirschvink, 1982; Stolz et al., 1986; Petersen et al., 1986), which are called “magnetofossils”. Magnetotactic bacteria are considered to be microaerophilic to anaerobic organisms that live near and below the oxic-anoxic transition zone (OATZ) of sedimentary columns with strong chemical gradients (Bazylinski and Moskowitz, 1998; Kopp and Kirschvink, 2007). With the recent progress of rock magnetic techniques such as first-order reversal curve (FORC) diagrams, it is now possible to detect the existence of biogenic magnetite in sediments (Egli et al., 2010; Li et al., 2012). As the result, the occurrence of biogenic magnetites has been recognized widely in deep-sea sediments (e.g., Yamazaki, 2008, 2009; Abrajevitch and Kodama, 2009; Kind et al., 2011; Roberts et al., 2011a; Larrasoaña et al., 2012; Roberts et al., 2012; Yamazaki, 2012; Roberts et al., 2013). However, previous studies were mostly for calcareous or siliceous sediments in relatively high-productivity provinces, which have the OATZ at relatively shallow depths within sediments, and oxic red clay in extremely low-productivity provinces was not studied well. If magnetotactic bacteria prefer strong chemical gradients, oxic red clay is not suitable for living for magnetotactic bacteria.

I have conducted a paleomagnetic and environmental rock-magnetic study of red clay cores of the Integrated Ocean Drilling Program (IODP) Site U1365 in the SPG (Figure 1-2), which cover the entire Cenozoic. First, I construct an age model using magnetostratigraphy and inter-core correlation. Then, I present that biogenic magnetites are dominant magnetic minerals in red clay. I discuss long-range paleoceanographic changes using environmental magnetic techniques. I also discuss relation between magnetic properties and ΣREY contents. There was no environmental magnetic study in the South Pacific Gyre before.

2. Geological setting and Materials

IODP Site U1365 cores were taken during the IODP Expedition 329 (Figure 1-2). The aim of the Expedition 329 was to investigate life beneath the seafloor of the SPG, where biological productivity is the lowest on the Earth (Figure 2-1), and total seven sites were occupied (Expedition 329 Scientists, 2011). The expedition of the R/V *JOIDES Resolution* started in Papeete, Tahiti, on 8 October 2010 and ended in Auckland, New Zealand, on 13 December. I joined the expedition as an onboard paleomagnetist.

Site U1365 (23º51.0S, 165º38.7W, water depth 5696 m) is located at the western edge of the SPG (Figures 1-2). This site is within a region of abyssal hill topography trending roughly east-west (085º), with reliefs ranging from 150 to 200 m. Red clay cores of 75.5 m long accumulated above the basaltic basement of about 125.5 Ma were recovered with an Advanced Piston Corer (APC). Pacific plate motion models indicate that this site has been within the SPG since about 80 Ma (Expedition 329 Scientists, 2011) (Figure 2-2). Site U1365 is reoccupation of DSDP Site 596. The sediments obtained at Site 596 had large gaps and were strongly disturbed. At Site 596, no onboard or post-cruise paleomagnetic measurements were conducted. At Site U1365, continuous and high-quality cores were recovered.

The sediments at Site U1365 consist primarily of clay, chert, and porcellanite (Expedition 329 Scientists, 2011) (Figure 2-3). The chert and porcellanite layers occur at depths from approximately 44 to 61.5 m. The principal components of the clay are clay minerals, zeolite, and red-brown to yellow-brown semiopaque oxide (RSO). Preliminary onboard X-ray diffraction (XRD) results of the clay minerals indicate that their principal components are smectite and mica

groups (Expedition 329 Scientists, 2011). The sediments at Site U1365 do not contain either calcareous or siliceous microfossils in general. Thus, precise age control with microfossils is difficult to be done. However, fish teeth (ichthyolith) suggest an Oligocene or Eocene age at a depth of 13 mbsf, and a Late Cretaceous age is estimated from radiolarians at 44 mbsf (Expedition 329 Scientists, 2011) (Figure 2-3). These results indicate extremely slow sedimentation at this site.

It is estimated that in the SPG oxygen penetrates down to the sediment-basalt interface through the entire sediment column (Fischer et al., 2009). At Site U1365, dissolved oxygen concentrations are higher than 50 μM throughout the sedimentary column (Expedition 329 Scientists, 2011) (Figure 2-4); this indicates that there is no OATZ in the sediments.

3. Methods

3.1. Magnetostratigraphy

Onboard paleomagnetic measurements

During the Expedition 329, archive half cores from Site U1365 were measured onboard *JOIDES Resolution* using a three-axis pass-thorough cryogenic magnetometer (2G Enterprises model 760). The measurements were conducted at 2.5 cm intervals before and after alternating field (AF) demagnetization with peak fields of 10 and 20 mT. The data from intervals with drilling disturbance (e.g., soupy sediments in Section 329-U1365A-3H-1) and fractured chert rubbles (Cores 329-U1365A-6H through 21H in Figure 2-3) were removed based on onboard

visual core descriptions (Expedition 329 Scientists, 2011). In addition, 43 discrete sediment samples (7 cm^3 cubes) taken at an interval of one per core section of 1.5 m long from all cores except for chert layers were analyzed. Of these, 24 were measured onboard for natural remanent magnetization (NRM) before and after AF demagnetization at peak fields of 10 and 20 mT using the pass-through magnetometer. The rest of the discrete samples were measured on land after the expedition as described below.

The Flexit core orientation tool was deployed for Cores 329-U1365A-1H through 4H (Expedition 329 Scientists, 2011). The Flexit tool was used in combination with nonmagnetic core barrels. Below Core 4H, cores were collected using a steel core barrel without the Flexit tool to avoid damaging the tool or nonmagnetic barrels on hard lithologies.

Post-cruise sampling and measurements

For obtaining detailed paleomagnetic and rock-magnetic records from the Site U1365 cores, I conducted high-resolution sampling of the upper part of the cores from 0 to 13 mbsf at the IODP Core Repository in the Texas A&M University in 2011. Sixty-one cubic samples with 7 cm^3 in volume were taken at an interval of 20 cm, and 170 cubic samples with 1 cm^3 in volume were taken at an interval of 8 cm.

I conducted paleomagnetic measurements of these 235 samples, as well as the 24 discrete samples that were not measured onboard. Remanent magnetizations were measured with a 2G model 760 pass-through cryogenic magnetometer system in a magnetically shielded room at the Geological Survey of Japan (GSJ), National Institute of Advanced Industrial Science and Technology (AIST). The samples of 7 cm^3 were subjected to stepwise thermal demagnetization. A

thermal demagnetizer of Sogo model Fine TD-30 were used. The heating steps were 100, 120, 150, 200, 250, 300, 350, 400, 450, 500, 550, 600, 650, and 700 ºC. Samples were heated in air. When wet samples dried, they shrank almost isotropically without serious deformation or cracking. The samples of 1 cm^3 cubes were subjected to stepwise AF demagnetization. The peak AF field steps were 5, 10, 15, 20, 25, 30, 35, 40, 50, 60, 70, and 80 mT.

3.2. Environmental rock-magnetism

S ratios and k_{ARM}/SIRM

Anhysteretic remanent magnetization (ARM) with a peak AF field of 80 mT and a direct-current (DC) bias field of 0.1 mT was imparted to the samples used for NRM measurements, and measured using the cryogenic magnetometer system of GSJ. ARM susceptibility (k_{ARM}) was calculated by normalizing ARM intensity with the strength of the DC field. Next, an isothermal remanent magnetization (IRM) was imparted to the samples in a 2.5 T inducing field using a pulse magnetizer (2G Enterprises model 660) at GSJ. Here the IRM acquired in a 2.5 T field is regarded as saturation IRM (SIRM). IRMs of 0.1 and 0.3 T were then successively imparted in the direction opposite to the initial IRM. The IRMs were measured using a spinner magnetometer (Natsuhara-Giken SMM-85) at GSJ. S ratios ($S_{-0.1T}$ and $S_{-0.3T}$) were calculated according to the definition of Bloemendal et al. (1992). $S_{-0.1T}$ is a ratio of low-coercivity to middle- and high-coercivity magnetic minerals. $S_{-0.3T}$ is a ratio of low- and middle coercivity to high coercivity magnetic minerals. Low, middle, and high coercivity minerals are typified by magnetite, maghemite, and hematite, respectively.

The ratio of ARM susceptibility to SIRM (k_{ARM}/SIRM) is widely used as a proxy for magnetite grain-size variations. k_{ARM} /SIRM decreases with increased average magnetic grain size (e.g., Banerjee et al., 1981; King et al., 1982), because ARM acquisition is enhanced for grains in the single-domain (SD) size range, in particular in the finer part of the SD range. The k_{ARM} /SIRM ratio is also sensitive to the relative abundance of biogenic magnetite and terrigenous magnetic minerals (Egli, 2004a; Yamazaki, 2008; Yamazaki and Ikehara, 2012; Yamazaki et al., 2013). Biogenic magnetite has fine grain size with a narrow distribution confined within the SD size range (tens of nanometers) and negligible magnetostatic interactions among intact chains of biogenic magnetosomes, whereas terrigenous magnetic minerals have a wider grain-size distribution and significant magnetostatic interactions among grains. ARM acquisition efficiency decreases with increasing magnetostatic interaction (Sugiura, 1979). Thus k_{ARM}/SIRM increases with increasing proportion of biogenic magnetite (Yamazaki et al., 2008).

FORC diagrams

Recently, first-order reversal curve (FORC) diagrams are widely used to characterize magnetic grain assemblages (Roberts et al., 2000; Yamazaki, 2008, 2009; Roberts et al., 2011; Yamazaki et al., 2013; Chen et al., 2014, Roberts et al., 2014). They provide information on the distribution of coercivities (H_c) and local interaction fields (H_u) for a magnetic grain assemblage. For example, they are used for detecting biogenic magnetites in sediments from the characteristic magnetic signal for a chain structure of magnetofossils, which has a sharp ridge along the Hc axis with little vertical spread (e.g., Chen et al., 2007; Egli et al., 2010; Heslop and Roberts, 2012).

FORC measurements were made on dried sediments using an alternating gradient magnetometer (AGM; MicroMag 2900, Princeton Measurements Corporation) at GSJ. Total 54 samples were measured at about 20 cm intervals from 0 m to 13 m, and about 1.5 m intervals in the rest. In the high-resolution measurements, the field spacing between measurements was set to 0.5 mT, and 192 FORCs were measured, with interaction field (H_u) between -15 and 15 mT and coercivity (H_c) from 0 to 60 mT. The maximum applied field was 1.4 T. The averaging time for each data point was 200 ms. In the low-resolution measurements, the field spacing between measurements was set to 1.3 mT, and 150 FORCs were measured, with interaction field (H_u) between -50 and 50 mT and coercivity (H_c) from 0 to 120 mT. I used a smoothing factor (Roberts et al., 2000) of 3. The FORCinel software (Harrison and Feinberg, 2008) was used for data processing.

IRM component analysis

IRM acquisition curves were measured using the AGM to estimate magnetic mineral compositions. The experiments were conducted on the same specimens used for the FORC measurements. One hundred measurements were made at equidistant field steps on a log-scale ranging form 3 mT to 1.4 T. The IRM acquisition curves were decomposed into magnetic coercivity components using the method of Kruiver et al, (2001) assuming that the IRM acquisition curves are a linear addition of components represented by cumulative log-Gaussian functions. This method is a kind of forward modeling, and hence there is arbitrariness for the choice of the number of components and a mean coercivity and dispersion parameter (DP) of individual components. For pelagic sediments in the Pacific Ocean, IRM acquisition curves are

described in general by two dominant components, a low-coercivity (L) component with a mean coercivity of ~40 mT and DP of ~0.2 and a middle-coercivity (M) component with a mean coercivity of ~100 mT and DP of ~0.3, and two other components, a very low-coercivity (VL) component with a mean coercivity of ~15 mT and a high-coercivity (H) component with a mean coercivity of >0.4 T (Yamazaki, 2008, 2009, 2012; Yamazaki and Ikehara, 2012). In this study, I at first adopted components with mean coercivities and DPs similar to those in the Pacific pelagic sediments, and examined if the observations were satisfied with changing their relative abundance, but without greatly changing the mean coercivities and DPs of individual components.

Low-temperature magnetic measurement

Low-temperature magnetic property measurements were done with a low-temperature susceptometer (Quantum Design MPMS-XL-5) at GSJ and the Center for Advanced Marine Core Research (CMCR), Kochi University. The main objective of the measurements was to investigate the mineralogy of red clay utilizing the phase transition of magnetite at approximately 120 K, known as the Verwey transition (Verwey, 1939). An abrupt loss of the remanent magnetization at this point is diagnostic of the presence of magnetite. Partial oxidation of magnetite significantly influences the Verwey transition. Oxidation to z = 0.3 essentially suppresses the transition (Özdemir et al., 1993). In fine-grained magnetite, oxidation of only the surface of the grains can inhibit the Verwey transition.

In the measurements, SIRM of 2.5 T was first imparted to a dried sample at 300 K, then cooled to 6 K and warmed up again to 300 K in an approximately zero field. Remanent magnetization was measured every 2 K during cooling and warming. Second, an IRM was

imparted to the specimens at a field of 2.5 T at 6 K after cooling in a zero field, which was followed by measurement of the SIRM during warming up to 300 K.

High-temperature magnetic measurement

Temperature dependence of saturation magnetization above room temperature provides information about magnetic mineralogy through Curie temperatures and inversion temperatures (Dunlop and Özdemir, 1997). Ten samples were measured using a magnetic balance (Natshara-Giken NMB-89) at CMCR, Kochi University. The specimens were heated from 30 to 700 ºC and cooled back to 30 ºC in air at a rate of 10 ºC min^{-1}. The inducing magnetic field was 0.5 T.

Observation with transmission electron microscope (TEM)

Magnetic minerals were observed with a transmission electron microscope (TEM, Topcon EM002B) at AIST. To extract magnetic minerals, sediments were completely dispersed in fresh water with sodium hexametaphosphate using an ultrasonic bath, and magnetic minerals were collected by circulating the dispersed sediments through a high magnetic field gradient. The magnetic extracts were dispersed in ethanol, and a small drop of the suspension was dried on a carbon-coated copper grid for TEM observations. The samples were examined with the TEM operating at 120 keV.

Magnetites of bacterial origin can be identified based on the characteristic morphologies (octahedron, parallelepiped, and tear-drop shape), size within the SD range, that is, several tens of nanometer, and alignment of grains in a chain (Petersen et al., 1986; Stolz et al., 1986; Kopp and

Kirschvink, 2007).

3.3. Rare earth element contents

Forty-three samples of 7 cm^3 cubes after rock-magnetic measurements were dried at 80 ºC for 24 hours and powdered in an agate mortar. After drying the powdered samples at 150 °C for about several hours, 0.05 g subsamples were dissolved in tightly sealed Teflon PFA screw-cap beakers with HNO_3–HF–$HClO_4$ digestion by heating in ovens at 140 °C for 12 hours, then at 150 °C for 12 hours. The dissolved samples were dried on a hot plate at 110 °C for 12 hours, then 160 °C for 6 hours. The residues were then dissolved with 4 mL of HNO_3 and 1 mL of HCl, and the solutions were diluted to 1:200 by mass.

Concentrations of fifteen rare earth elements (La, Ce, Pr, Nd, Pm, Sm, Eu, Gd, Tb, Dy, Ho, Er, Th, Yb, and Lu) and Yttrium (ΣREY) were analyzed with an inductively-coupled plasma-mass spectrometer (ICP-MS, Agilent 7500ce) at the Japan Agency for Marine-Earth Science and Technology (JAMSTEC). Two reference materials provided by GSJ, AIST, were used for calibration: JB-2 (basalt) (Imai et al., 1995) and JMS-2 (deep-sea pelagic sediments) (Terashima et al., 2002).

4. Results

4.1. Age model

Magnetostratigraphy

Magnetic polarity interpretations are shown in Figure 4-1 and Table 4-1. The present-day normal polarity field expected from the geocentric axial dipole model at the site has a negative inclination (approximately -41.5°). From the onboard pass-thorough measurements, I could interpret the magnetic polarities down to about 6 mbsf after AF demagnetization at a peak field of 20 mT. The Brunhes/Matuyama (B/M) chron boundary (0.78 Ma; Gradstein et al., 2004) is at approximately 1.8 mbsf. The Matuyama/Gauss (M/G) chron boundary (2.59 Ma) is at approximately 4.0 mbsf. The Gauss/Gilbert chron boundary (3.58 Ma) is at approximately 4.4 mbsf.

The interpretation from the onboard preliminary measurements is supported by the post-cruise measurements (Figure 4-1). Figure 4-2 shows typical examples of the results of stepwise AF and thermal demagnetizations above 6 mbsf. The stepwise AF demagnetization indicates the presence of a stable, well-defined characteristic remanent magnetization (ChRM). Secondary magnetization that was probably acquired during coring, which is sometimes serious for ODP/IODP APC cores (e.g., Herr et al., 1998), could generally be removed by peak fields of 5 to 15 mT. The ChRMs, which were determined using principal component analysis (Kirschvink, 1980), have maximum angular deviation (MAD) values that are generally within 10 degrees except for stratigraphic intervals associated with polarity transitions. On the thermal demagnetization, secondary magnetizations could be removed by demagnetization up to 400 ºC (Figure 4-2). Directions of the ChRM are consistent between thermal and AF demagnetizations. Ages were assigned to the cores by correlating polarity boundaries to the geomagnetic polarity time scale of Gradstein et al. (2004), and the results are similar to those based on the shipboard half-core measurements. From this polarity interpretation, a sedimentation rate is approximately

1.7 m/m.y. during the Brunhes Chron (the last 0.78 m.y.), and it decreases downcore to about 0.6 m/m.y. at 6 mbsf (Figure 4-3). It is not necessary to consider the influence of compaction after accumulation for the sedimentation rate calculation because density and porosity hardly change with depth in the studied cores (Expedition 329 Scientists, 2011).

Below about 6 mbsf, on the other hand, secondary magnetizations could not be removed with either AF or thermal demagnetizations (Figure 4-4), and magnetic polarities are not interpretable (Figures 4-5). The secondary magnetizations may have been caused by magnetic overprints acquired during coring (high positive inclination), a viscous remanent magnetization, or diagenetic changes in the sediments.

Age estimation from DSDP Site 596

The ages of the Site U1365 cores below 6 mbsf were transferred from those of Site 596 by inter-core correlations using magnetic susceptibility and ΣREY content variation patterns. The position of Site 596 is almost the same as that of Site U1365, and the core lithology coincides with each other. The age model of Site 596 was established by Zhou and Kyte (1992), which was based mainly on a constant Cobalt flux model. This model also incorporated a preliminary biostratigraphic analysis based on ichthyolith (Winfrey et al., 1987).

Magnetic susceptibility of Site U1365 cores was measured onboard using a whole-round multisensor logger (WRMSL) (Expedition 329 Scientists, 2011) (Figure 4-6). Magnetic susceptibility of Site 596 samples were measured with a Bartington MS2 susceptmeter using samples remained after ΣREY analysis of Kato et al. (2011) (T. Yamazaki, unpublished). Values of magnetic susceptibility at Site U1365 are higher than about 5.0×10^{-4} SI in general except for

the chert and porcellanite layers (Figure 4-6). There are a narrow peak between about 4.5 and 7.5 mbsf (3.2×10^{-3} SI at the maximum at 6.0 mbsf) and a broad increase between about 24 and 44 mbsf (1.2×10^{-3} SI at the maximum at 33.0 mbsf). Below the chert layers at 62.0 mbsf, magnetic susceptibility is relatively lower than that of the upper part of the cores.

ΣREY contents are high, above 500 ppm, below 8.0 mbsf, and extremely high, about 1280 ppm on average between about 8 and 38 mbsf (Figure 4-7). The maximum value is about 2470 ppm at 10.1 mbsf, which is higher than the maximum, about 2110 ppm, reported by Kato et al. (2011) at Site 596. My measurement intervals are denser than those of Kato et al. (2011).

A magnetic susceptibility peak at approximately 6.0 m and lows at 1.1 and 8.0 m of Site U1365 were correlated with a peak at approximately 6.0 m and lows at 1.4 and 13 m of Site 596, respectively (Figure 4-7). Total REY peaks at 17.8 and 34.0 m and lows at 22.2, 36.0, and 41.0 m of Site U1365 were correlated with peaks at 17.6 and 34.0 and lows at 21.5, 41.0, and 47.0 m of Site 596, respectively (Figure 4-7). Variations of magnetic susceptibility and ΣREY content at Sites U1365 and 596 agree well on the age axis (Figure 4-8). The age of the ΣREY peak is about 35 Ma.

4.2. Environmental rock magnetism

FORC diagrams

All high-resolution FORC diagrams have a narrow ridge along the H_c axis at $H_u = 0$ (Yamazaki and Shimono, 2013), which indicates negligible magnetostatic interactions (Roberts et al., 2000) (Figure 4-9). This is a characteristic of biogenic magnetite, called “the central ridge”

(Egli et al., 2010; Roberts et al., 2011, 2012; Li et al., 2012; Yamazaki, 2012; Yamazaki and Ikehara, 2012; Roberts et al. 2014).

Above about 8.0 mbsf, a weak and broad signal with considerable vertical spread along the H_u axes is recognized on the FORC diagrams in addition the central ridge (Figures 4-9). This broad component is inferred to be carried by a mixture of interacting SD and pseudo-single domain (PSD) grains (Roberts et al., 2000; Pike et al., 2001). On the low-resolution FORC diagrams with a wider H_u range, FORC distributions of the broad component tend to diverge from the $H_u = 0$ axis (Figure 4-10), which is interpreted to be carried mainly by multi-domain (MD) grains (Roberts et al., 2000; Pike et al., 2001). The broad component with significant magnetostatic interactions contrasts with the central-ridge component representing biogenic magnetite, and it is inferred to be of terrigenous origin (Yamazaki, 2008, 2009; Yamazaki and Ikehara, 2012). Below about 8.0 mbsf, only the central ridge is visible on the FORC diagrams (Figure 4-9). These results suggest that biogenic magnetites are a dominant consistent of magnetic mineral assemblages throughout the sediment column, in particular below about 8.0 mbsf.

k_{ARM}/SIRM ratio

k_{ARM}/SIRM ratio suddenly increases downcore at about 8.0 mbsf from about 0.5 to 2×10^{-3} m/A (Figure 4-11). This indicates that the proportion of biogenic magnetite to terrigenous magnetic minerals increases there. High k_{ARM}/SIRM ratios, about 1.0×10^{-3} m/A or higher, suggest dominance of biogenic magnetite (Egli, 2004a; Kobayashi et al., 2006; Li et al., 2012). The high k_{ARM}/SIRM ratios of Site U1365 are consistent with the predominance of biogenic

magnetite inferred from the prominent central ridge on the FORC diagrams, in particular below about 8.0 mbsf (Yamazaki and Shimono, 2013).

IRM component analysis

IRM component analyses revealed that IRM is carried mainly by a low-coercivity component, with a mean coercivity of approximately 35 mT and a relatively small dispersion parameter of 0.2 (Yamazaki and Shimono, 2013) (Figure 4-12). I interpret that the low-coercivity (L) component corresponds to the biogenic soft component of Egli (2004a) representing biogenic magnetite with isotropic morphology from its coercivity and k_{ARM}/SIRM values, and that it corresponds to the non-interacting SD component constituting the central ridge on the FORC diagrams (Yamazaki, 2009; Yamazaki and Ikehara, 2012). A middle-coercivity (M) component with a mean coercivity of approximately 100 mT and a dispersion parameter of approximately 0.3 appears in the uppermost several meters at Site U1365 (Figure 4-12) and is interpreted to reflect terrigenous maghemite transported as eolian dust (Yamazaki 2009; Yamazaki and Ikehara, 2012). In addition, optimal fitting to the data requires a very low-coercivity component, which probably reflects coarse PSD and/or MD grains. The biogenic (L) and terrigenous (M) components, with mean coercivities and dispersion parameters similar to those observed in the red clay samples, are commonly observed in pelagic sediments in the Pacific and Indian Oceans (Yamazaki, 2009; Roberts et al., 2011; Yamazaki, 2012; Yamazaki and Ikehara, 2012).

The proportion of magnetization carried by the M component changes remarkably with depth. Above about 8.0 m the proportion of the M component increases upcore. Below about 8.0 m, on the other hand, the M component disappears (Figures 4-12).

S ratios

$S_{-0.3T}$ values are high, about 0.97 or higher. This indicates that the contribution of high-coercivity minerals such as hematite to SIRM is very small (Figure 4-13 right). This result is consistent with that there is no high-coercivity component in the IRM component analyses. $S_{-0.1T}$ values below about 8.0 mbsf are close to 1.0, which indicates the dominance of low-coercivity minerals such as magnetite (Figure 4-13 left). Above about 8.0 mbsf, $S_{-0.1T}$ decreases upcore to about 0.84. This suggests an upcore increase of middle-coercivity minerals like maghemite. This is consistent with result of the IRM component analyses, that is, the upcore increase in the M component above about 8.0 mbsf (Figure 4-12).

Low-temperature magnetic measurement

Thermal demagnetization curves of SIRM acquired at 6 K do not show an abrupt decrease around 120 K expected for the Verwey transition of magnetite (lower panels of Figure 4-14). However, low-temperature cycling of room-temperature SIRM shows difference between cooling and warming curves (upper panels of Figure 4-14). This difference suggests the presence of magnetite. I infer that the surface of the magnetite was oxidized to maghemite. Partial oxidation of magnetite is known to suppress the Verwey transition (Özdemir et al., 1993).

High-temperature magnetic measurement

The thermomagnetic curves for all samples show irreversible behavior during cooling (Figure 4-16). Magnetization during cooling is lower than that during heating in general. This can be

explained by that maghemite, which is known to become unstable at temperature higher than about 400ºC, was decomposed and oxidized to hematite in air. The presence of maghemite is consistent with the presence of the M component in the IRM component analyses and no visible Verwey transition in the low-temperature measurements.

Observation with transmission electron microscope (TEM)

On the TEM observations, biogenic magnetite was identified based on the characteristic morphologies, size within the SD range (i.e. several tens of nanometers), and the alignment of grains in chains (Petersen et al., 1986; Stolz et al., 1986; Kopp and Kirschvink, 2007) (Figure 4-16). TEM images indicate that biogenic magnetite is abundant and that the dominant morphology is octahedral (>90%) with a minor occurrence of elongated prisms (Figure 4-16(e)) (Yamazaki and Shimono, 2013). Grains with dendritic shapes (Figure 4-16(b)), which probably originated from weathered micrometeorites, are also frequently observed. This is consistent with the low sedimentation rates.

5. Discussion

Biogenic magnetite in red clay

This study revealed that biogenic magnetite dominates magnetic mineral assemblages in oxic red clay devoid of the OATZ, implying habitation of magnetotactic bacteria there (Yamazaki and Shimono, 2013). This results conflict with the current thoughts that magnetotactic bacteria seek a preferable position in a strong vertical chemical gradient (Bazylinski and Moskowitz, 1998;

Bazylinski and Frankel, 2004) and that magnetotaxis is for efficient search of the preferable position utilizing the geomagnetic field (Kirschvink, 1980; Frankel et al., 1997). It was previously reported in pelagic and hemipelagic sediments of the eastern South Atlantic Ocean that detection of actively swimming magnetotactic bacteria is limited at water depths shallower than about 3000 m (Petermann and Bleil, 1993). However, this result does not exclude a possibility of habitation of magnetotactic bacteria in red clay. In sediments of extremely slow deposition like red clay, it is inferred that concentration of biogenic magnetite can become high in a long period of time even if population of living magnetotactic bacteria is too small to be observed. It is consider that biogenic magnetite in red clay are not provided from water column above the seafloor. In strongly anoxic environments like blackish lakes, the OATZ occurs within a water column and magnetotactic bacteria live there, but the SPG is not in such anoxic conditions. The bathyal oxygen minimum zone (OMZ), which occurs at about 1000 m below sea surface in general, might be habitable for magnetotactic bacteria, but in the SPG dissolved oxygen contents are still high at the OMZ (Paulmier and Ruiz-Pino, 2009).

Most biogenic magnetites found in red clay have octahedral morphology (Figure 4-16). This is in marked contrast to biogenic magnetites in higher productivity provinces like the southern Ocean and equatorial zones, which is a mixture of octahedral and elongated morphologies (Yamazaki, 2012; Yamazaki and Ikehara, 2012). Previous studies suggested that the proportion of biogenic magnetites with elongated morphologies increases in less oxic environments (Hesse, 1994; Yamazaki and Kawahata, 1998; Egli, 2004b; Yamazaki, 2012; Yamazaki and Ikehara, 2012), which is consistent with the observation that octahedral morphology dominates biogenic magnetites in red clay. The regional differences in morphological constituent indicate that

biogenic magnetites in red clay are *in situ* and were not transported from equatorial zones or high latitudes by bottom currents.

Cenozoic environmental change

It was revealed that the input of terrigenous magnetic minerals, which is estimated to be transported as eolian dust, has increased since about 35 Ma at Site U1365 (Figures 5-1 and 5-2). The k_{ARM}/SIRM values, a proxy for the proportion of biogenic to terrigenous components, have decreased since about 35 Ma (Figure 5-1(a)). The FORC diagrams show coeval increase of the interacting component (Figure 5-1(b)), which is estimated to be carried by terrigenous magnetic minerals. The proportion of the M component in the IRM component analyses has also increased since about 35 Ma; the increase accelerated after about 5 Ma (Figure 5-2(d)). The sedimentation rates have also dramatically increased since about 5 Ma (Figure 5-2(e)). Thus, eolian dust flux may have increased at two steps, at about 35 and 5 Ma.

I infer that the source of eolian dust at Site U1365 is Australia, because it has widest arid and semi arid areas in the Southern hemisphere and the site is under the lee of Australia. Figure 5-3 shows paleopositions of Site U1365 and Australia during the Cenozoic (present, 15, 35, and 55 Ma) based on past plate motion models using the Gplates software (Seton et al., 2012). At about 35 Ma, Australia entered into the arid area of middle latitudes. The Eocene-Oligocene boundary (about 34 Ma) is known as the time of a major global cooling, and large-scale glaciation was developed on Antarctica at this time (Zachos et al., 2001). The two major ocean gateways in the southern hemisphere, the Drake passage and Tasmanian gateway, opened and the Antarctic Circumpolar Current was formed at that time (Kennet et al., 1977; Scher and Marting, 2004,

2006; Stickley et al., 2004), which is thought to be responsible for the cooling (Scher and Marting, 2006). The global cooling would have caused enlarged potential source areas of eolian dust and stronger atmospheric circulation, which resulted in increased eolian dust flux.

The second increase of eolian dust flux at about 5 Ma may have been caused by a further growth of the Antarctic glaciation at about 6 Ma (Barker and Kennett, 1988; Kennett and Barker; 1990). As mentioned in chapter 4.1, magnetostratigraphy could not be established below about 6 mbsf (before about 5 Ma) due to unstable remanent magnetization. In the Northern hemisphere, on the other hand, an increase of eolian dust flux is known to have occurred at about 3 Ma (Rea, 1994), which is considered to be caused by the onset of the Northern hemisphere glaciation at this time. In the red clay province in the NPG, it is known that remanent magnetization is unstable before about 3 Ma (Kent and Lowrie, 1974; Yamazaki and Ioka, 1997). The unstable-to-stable transition of remanent magnetization in the SPG, about 5 Ma, is older than that in the NPG. For both the NPG and SPG, the ages of the unstable-to-stable transition seem to coincide with the ages of the increase in eolian dust flux. This coincidence suggests that terrigenous magnetic minerals transported as eolian dust carry stable remanent magnetization. This study revealed that in red clay provinces magnetotactic bacteria may live anywhere in sedimentary columns and leave "young" biogenic magnetite in deeper parts because there is no OATZ and thus no chemically particularly preferable position for magnetotactic bacteria. If magnetotactic bacteria can live deep in red clay, biogenic magnetite should cause magnetic overprint.

Relation of magnetic properties and ΣREY contents

The ΣREY content variation pattern resembles k_{ARM}/SIRM variations (Figure 5-2(b)(c)). The ΣREY content peak occurs just before the rapid decrease in k_{ARM}/SIRM at about 35 Ma. An interval of high magnetic susceptibility occurs after a decrease in ΣREY content (Figure 5-2(a)). These rock-magnetic and ΣREY content characteristics at Site U1365 are similar to those observed in red clay cores taken near Minami-Torishima in the northwest Pacific (Yamazaki et al., 2014) (Figure 5-4). Although an age model has not yet been established for the red clay cores near Minami-Torishima, a peak of ΣREY content occurs near the k_{ARM}/SIRM shift and before the interval of high magnetic susceptibility (Figure 5-4). The observation that the relation of ΣREY content peaks and magnetic property changes coincides at the two sites of a wide expanse may suggest that the increased ΣREY concentration was occurred in association with a paleoceanographic event near the Eocene-Oligocene boundary.

For the cause of the high-ΣREY contents in red clay, Kato et al. (2011) suggested that it is due to uptake of rare-earth elements and yttrium by hydrothermal iron-oxyhydroxides and phillipsite, and that it is related to the hydrothermal activity along the East Pacific Rise (EPR). On the other hand, Kon et al. (2014) conducted a geochemical and mineralogical investigation of the ΣREY-rich red clay near Minami-Torishima. They concluded that the main ΣREY host phase is fish debris apatite. I infer that the hydrothermal activity along the EPR is not a dominant controlling factor for ΣREY contents in red clay, because Site U1365 and the sites near Minami-Torishima are not close to the EPR. There is no evidence that the hydrothermal activity along the EPR reduced since about 35 Ma. Instead, deposition and abundance of fish debris apatite may have been affected by paleoceanographic events, which may have influenced ΣREY concentration.

6. Conclusions

The paleomagnetic and rock-magnetic analyses of this study on red clay at IODP Site U1365 in the SPG have led the following conclusions.

1. Magnetostratigraphy could be established above about 6 mbsf (about 5 Ma). Before about 5 Ma, magnetic polarities were not interpretable due to unstable magnetization. The age of the unstable-to-stable transition of remanent magnetization is older than that in the NPG. The age of the unstable-to-stable transition seems to coincide with that of the increase in eolian dust flux. Below about 6 mbsf, the ages of the Site U1365 cores were transferred from published ages of nearby DSDP Site 596, which is based mainly on a constant Cobalt flux model, by inter-core correlation using magnetic susceptibility and ΣREY content variation patterns.

2. Magnetic minerals in red clay at Site U1365 mainly consist of partially oxidized biogenic magnetite and terrigenous maghemite. Although there is no OATZ at Site U1365, biogenic magnetites dominate magnetic mineral assemblages throughout the sedimentary column. This conflicts with the current thoughts that magnetotactic bacteria live in a strong vertical chemical gradient near the OATZ. Magnetotactic bacteria may live anywhere in sedimentary columns of red clay.

3. Terrigenous magnetic minerals increased since about 35 Ma, and the increase accelerated after 5 Ma. The causes of the increased terrigenous input are considered to be northward shift of Australia and Site U1365 to an arid region and cooling of the Southern hemisphere near the Eocene-Oligocene boundary and at about 5 Ma.

4. ΣREY content variation pattern resembles that of k_{ARM}/SIRM, which is a proxy of the biogenic to terrigenous magnetic components. Moreover, rock-magnetic and ΣREY content variation patterns at Site U1365 are similar to those of red clay cores near Minami-Torishima in the northwest Pacific. This suggests that the enhanced ΣREY concentration may have occurred in association with a common paleoceanographic event.

7. Acknowledgements

The author would like to express sincere thanks to Profs. Toshitsugu Yamazaki and Akira Takada for guidance and encouragement. I greatly appreciate the help I received from Prof. Ken-ichiro Hisada and Dr. Ryo Anma. I would like also to thank Drs. Katsuhiko Suzuki, Ryoko Senda, and Saori Kubo for help with rare earth content measurements, and Dr. Akira Takatsuki for help with transmission electron microscope (TEM) observations. The cores used in this study were obtained through the cooperation of all onboard scientists, marine technicians, officers, and crew of the IODP Expedition 329 of D/V *JOIDES Resolution*. This research used samples provided by the IODP. My participation to the Expedition 329 was supported by the Japan Drilling Earth Science Consortium and the Center for Deep Earth Exploration, Japan Agency for Marine-Earth Science and Technology.

8. References

Abrajevitch, A., and K. Kodama (2009), Biochemical vs. detrital mechanism of remanence acquisition in marine carbonates: A lesson from the K–T boundary interval, *Earth Planet. Sci. Lett.*, *286*, 269–277, doi:10.1016/j.epsl.2009.06.035.

Behrenfeld, M.J., and P.G. Falkowski (1997), Photosynthetic rates derived from satellite-based chlorophyll concentration, *Limnology and Oceanography*, *42*, 1–20, doi:10.4319/lo.1997.42.1.0001.

Barker, P. F., and J. P. Kennett (1988), *Proc. ODP, Init. Repts.*, *113,* College station, TX (Ocean Drilling Program), doi: 10.2973/odp.proc.ir.113.1988.

Banerjee S. K., J. King, and J. Marvin (1982), A rapid method for magnetic granulometry with applications to environmental studies, *Gephys. Res. Lett.*, *8*, 333-336.

Bareille G., and F. E. Grousset, and M. Labracherie (1994), Origin of detrital fluxes in the southeast Indian Ocean during the last climatic cycles, *Paleoceanography*, *9*, 799-819.

Bazylinski, D. A., and B. M. Moskowitz, (1998), Microbial biomineralization of magnetic iron minerals: Microbiology, magnetism and environmental significance. In *Geomicrobiology: Interactions Between Microbes and Minerals*, *Mineral. Soc. Am., Washington D.C*, 181-223.

Bazylinski, D. A., and R. B. Frankel (2004), Magnetosome formation in prokaryotes, *Nat. Rev. Microbiol.*, *2*, 217–30, doi:10.1038/nrmicro842.

Blakemore, R. (1975), Magnetotactic bacteria, *Science*, *190*, 377–379, doi:10.1126/science.170679.

Blakemore, R. P. (1982), Magnetotactic bacteria, *Annu. Rev. Microbiol.*, *36*, 217–38, doi:10.1146/annurev.mi.36.100182.001245.

Blank, M., M. Leinen, and J. M. Prospero (1985), Major Asian aeolian inputs indicated by the mineralogy of aerosols and sediments in the western North Pacific, *Nature*, *314*, 84–86, doi:10.1038/314084a0.

Brown, J., A. Colling, D. Park, J. Phillips, D. Rothery, and J. Wright (1989), Ocean basins: their structure and evolution, *Open University*.

Chen, A. P., R. Egli, and B. M. Moskowitz (2007), First-order reversal curve (FORC) diagrams of natural and cultured biogenic magnetic particles, *J. Geophys. Res.*, *112*, B08S90, doi:10.1029/2006JB004575.

Chen, A. P., V.M. Berounsky, M.K. Chan, M.G. Blackford, C. Cady,w, B.M. Moskowitz, P. Kraal, E.A. Lima, R.E. Kopp, G.R. Lumpkin, B.P. Weiss, P. Hesse and N.G.F. Vella (2014), Magnetic properties of uncultivated magnetotactic bacteria and their contribution to a stratified estuary iron cycle., *Nat. Commun.*, *5*, 4797, doi:10.1038/ncomms5797.

Doh S. J., J. W. King, and M. Leinen (1988), A rock-magnetic study of giant piston core LL44-GPC3 form the central north Pacific and its paleoceanographic implications, *Paleoceanography, 3*, 89-111.

Dunlop, D.J, and Ö. Özdemir (1997), *Rock Magnetism: Fundamentals and Frontiers*, 573 pp., Cambridge Univ. Press, Cambridge.

Egli, R. (2004a), Characterization of Individual Rock Magnetic Components by Analysis of Remanence Curves, 1. Unmixing Natural Sediments, *Stud. Geophys. Geod.*, *48*, 391–446, doi:10.1023/B:SGEG.0000020839.45304.6d.

Egli, R. (2004b), Characterization of individual rock magnetic components by analysis of remanence curves, *Phys. Chem. Earth, Parts*, *29*, 851–867, doi:10.1016/j.pce.2004.04.001.

Egli, R., A. P. Chen, M. Winklhofer, K. P. Kodama, and C. S. Horng (2010), Detection of noninteracting single domain particles using first-order reversal curve diagrams, *Geochemistry, Geophys. Geosystems*, *11*, doi:10.1029/2009GC002916.

Evans, M. E., and F. Heller (2003), *Environmental Magnetism: Principles and Applications of Enviromagnetics*, 299 pp, Academic, San Diego, Calif.

Expedition 329 Scientists (2011), Site U1365, in D'Hondt, S. et al., *Proceedings of the Integrated Ocean Drilling Program*, *329*, Integrated Ocean Drilling Program Management International Inc., Tokyo.

Fischer, J. P., T. G. Ferdelman, S. D'Hondt, H. Røy, and F. Wenzhöfer (2009), Oxygen penetration deep into the sediment of the South Pacific gyre, *Biogeosciences, 6*, 1467–1478.

Frankel, R. B., D. A. Bazylinski, M. S. Johnson, and B. L. Taylor (1997), Magneto-Aerotaxis in Marine Coccoid Bacteria, *Biophys. J.*, *73*, 994–1000.

Gradstein, F.M., J.G.Ogg, and A. Smith, (2004), *A Geologic Time Scale 2004*, 589 pp., *Cambridge Univ. Press*, Cambridge.

Harrison, R. J., and J. M. Feinberg (2008), FORCinel: An improved algorithm for calculating first-order reversal curve distributions using locally weighted regression smoothing, *Geochemistry, Geophys. Geosystems*, *9*, doi:10.1029/2008GC001987.

Herr, B., M. Fuller, M. Haag, and F. Heider (1998), 6. Influence of drilling on two records of the Matuyama/Brunhes polarity transition in marine sediment cores near Gran Canaria, *Proc. ODP*, *157*, 57–69.

Heslop, D., and A. P. Roberts (2012), Estimation of significance levels and confidence intervals for first-order reversal curve distributions, *Geochem. Geophys. Geosyst.*, *13*, Q12Z40, doi:10.1029/2012GC004115.

Hesse, P. P. (1994), Evidence for bacterial palaeoecological origin of mineral magnetic cycles in oxic and sub-oxic Tasman Sea sediments, *Mar. Geol., 117*, 1-17.

Imai, N., S. Terashima, S. Itoh and A. Ando (1995), 1994 compilation of analytical data for minor and trace elements in seventeen GSJ geochemical reference samples, "Igneous Rock Series", *Geostand Newslett.*, *19*, 135-213, doi:10.1111/j.1751-908X.1995.tb00158.x

Janecek, T. R., and Rea (1980), Eolian deposition in the northeast Pacific Ocean: Cenozoic history of atmosphere circulation, *Geol. Soc. of Amer. Bull., 94,* 730-738.

Janecek, T. R., and L. G. Observatory of Columbia Univ. (1985), 26. Eolian sedimentation in the northwest Pacific Ocean: a preliminary examination of the data from Deep Sea Drilling Project Sites 576 and 578. *Proc. ODP*, *86*, 589–603.

Kato, Y., K. Fujinaga, K. Nakamura, Y. Takaya, K. Kitamura, J. Ohta, R. Toda, T. Nakashima, and H. Iwamori (2011), Deep-sea mud in the Pacific Ocean as a potential resource for rare-earth elements, *Nat. Geosci.*, *4*, 535–539, doi:10.1038/ngeo1185.

Kennett, J. P. (1977), Cenozoic evolution of Antarctic glaciation, the circum-Antarctic Ocean, and their impact on global paleoceanography, *J. Geophys. Res.*, *82*.

Kennett, J. P., and P. F. Barker (1990), 53. Latest Cretaceous to Cenozoic climate and oceanographic developments in the Weddell Sea, Antarctica: an ocean-drilling perspective, *Proc. ODP*, *113*, 937–960.

Kent, D. V., and W. Lowrie (1974), Origin of magnetic instability in sediment cores from the central North Pacific, *J. Geophys. Res.*, *79*, 2987–3000, doi:10.1029/JB079i020p02987.

Kind, J., A. U. Gehring, M. Winklhofer, and A. M. Hirt (2011), Combined use of magnetometry and spectroscopy for identifying magnetofossils in sediments, *Geochemistry, Geophys. Geosystems*, *12*, doi:10.1029/2011GC003633.

King, J., S. K. Banerjee, J. Marvin, and O. Ozdemir (1982), relative grain size of magnetite in natural materials: some results from lake sediments, *Earth Planet. Sci. Lett.*, *59*, 404–419.

Kirschvink, J. L. (1980a), The laeast-squares line and plane and the analysis of paleomagnetic data, *Geophys. J.R. astr. Soc., 62,* 699–718.

Kirschvink, B. Y. J. L. (1980b), South-seeking magnetic bacteria, *J. exp. Biol.*, *86*, 345–347.

Kirschvink, J. L. (1982), Paleomagnetic evidence for fossil biogenic magnetite in western Crete, *Earth Planet. Sci. Lett.*, *59*, 388–392, doi:10.1016/0012-821X(82)90140-6.

Kon, Y., M. Hoshino, K. Sanematsu, S. Morita, M. Tsunematsu, N. Okamoto, N. Yano, M. Tanaka, and T. Takagi (2014), Geochemical Characteristics of Apatite in Heavy REE-rich Deep-Sea Mud from Minami-Torishima Area, Southeastern Japan, *Resour. Geol.*, *64*, 47–57, doi:10.1111/rge.12026.

Kopp, R. E., and J. L. Kirschvink (2008), The identification and biogeochemical interpretation of fossil magnetotactic bacteria, *Earth-Science Rev.*, *86*, 42–61, doi:10.1016/j.earscirev.2007.08.001.

Kruiver, P. P., M. J. Dekkers, and D. Heslop (2001), Quantification of magnetic coercivity components by the analysis of acquisition curves of isothermal remanent magnetisation, *Earth Planet. Sci. Lett.*, *189*, 269-276.

Kyte, F. T., M. Leinen, G. Ross Heath, and L. Zhou (1993), Cenozoic sedimentation history of the central North Pacific: Inferences from the elemental geochemistry of core LL44-GPC3, *Geochim. Cosmochim. Acta*, *57*, 1719–1740, doi:10.1016/0016-7037(93)90109-A.

Larrasoaña, J. C., A. P. Roberts, L. Chang, S. a. Schellenberg, J. D. Fitz Gerald, R. D. Norris, and J. C. Zachos (2012), Magnetotactic bacterial response to Antarctic dust supply during the Palaeocene–Eocene thermal maximum, *Earth Planet. Sci. Lett.*, *333-334*, 122–133, doi:10.1016/j.epsl.2012.04.003.

Li, J., W. Wu, Q. Liu, and Y. Pan (2012), Magnetic anisotropy, magnetostatic interactions and identification of magnetofossils, *Geochemistry, Geophys. Geosystems*, *13*, Q10Z51, doi:10.1029/2012GC004384.

Mann S., N.H.C. Sparks, R. B. Frankel, Bazilinski, and H. W. Jannasch, (1990), Biomineralization of ferrimagnetic greigite (Fe_3S_4) and iron pyrite (FeS_2) in a magnetotactic bacterium, *Nature*, *343*, 258-261, doi:10.1007/BF01139266.

Özdemir, Ö., and D. J. Dunlop, and Moskowitz (1993), *20*(16), 1671–1674.Paulmier, a., and D. Ruiz-Pino (2009), Oxygen minimum zones (OMZs) in the modern ocean, *Prog. Oceanogr.*, *80*, 113–128, doi:10.1016/j.pocean.2008.08.001.

Petermann, H., and U. Bleil (1993), Detection of live magnetotactic bacteria in South Atlantic deep-sea sediments, *Earth Planet. Sci. Lett.*, *117*, 223–228, doi:10.1016/0012-821X(93)90128-V.

Pettke, T., A. N. Halliday, and D. K. Rea (2002), Cenozoic evolution of Asian climate and sources of Pacific seawater Pb and Nd derived from eolian dust of sediment core LL44-GPC3, *Paleoceanography*, *17*, 1–13, doi:10.1029/2001PA000673.

Pike, C. R., A. P. Roberts, M. J. Dekkers, and K. L. Verosub (2001), An investigation of multi-domain hysteresis mechanisms using FORC diagrams, *Phys. Earth Planet. Inter.*, *126*, 11–25, doi:10.1016/S0031-9201(01)00241-2.

Rea, D. K. (1994), The paleoclimatic record provided by eolian deposition in the deep sea: The geologic history of wind, *Rev. Geophys.*, *32*, 159, doi:10.1029/93RG03257.

Rex, R. W., and E. D. Goldberg (1958), Quartz Contents of Pelagic Sediments of the Pacific Ocean, *Tellus*, *10*(1), 153-159, doi:10.1111/j.2153-3490.1958.tb01995.x.

Roberts, A. P., C. R. Pike, and K. L. Verosub (2000), First-order reversal curve diagrams: A new tool for characterizing the magnetic properties of natural samples, *J. Geophys. Res.*, *105*, 461-475, doi:10.1029/2000JB900326.

Roberts, A. P., F. Florindo, G. Villa, L. Chang, L. Jovane, S. M. Bohaty, J. C. Larrasoaña, D. Heslop, and J. D. Fitz Gerald (2011), Magnetotactic bacterial abundance in pelagic marine environments is limited by organic carbon flux and availability of dissolved iron, *Earth Planet. Sci. Lett.*, *310*, 441–452, doi:10.1016/j.epsl.2011.08.011.

Roberts, A. P., L. Chang, D. Heslop, F. Florindo, and J. C. Larrasoaña (2012), Searching for single domain magnetite in the “pseudo-single-domain” sedimentary haystack:

Implications of biogenic magnetite preservation for sediment magnetism and relative paleointensity determinations, *J. Geophys. Res.*, *117*, B08104, doi:10.1029/2012JB009412.

Roberts, A. P., F. Florindo, L. Chang, D. Heslop, L. Jovane, and J. C. Larrasoaña (2013), Magnetic properties of pelagic marine carbonates, *Earth-Science Rev.*, *127*, 111–139, doi:10.1016/j.earscirev.2013.09.009.

Roberts, A. P., D. Heslop, X. Zhao, and C. R. Pike (2014), Understanding fine magnetic particle systems through use of first-order reversal curve diagrams, *Rev. Geophys*., *53*, 557-602, doi:10.1002/2014RG000462

Seton, M., R. D. Müller, and S. Zahirovic, T. Torsvik, G. Shephard, A. Atlsma, M. Gunis, and C. Gaina (2012), Global continental and ocean bain reconstructions since 200 Ma, *Earth-Science Reviews*, *37*, 212–270, doi:10.1016/j.earscirev.2012.03.002.

Scher, H. D., and E. E. Martin (2006), Timing and Climatic Consequences of the Opening of Drake Passage, *Science*, *312*, 428–430.

Schmieder F., T. von Dobeneck, and U. Bleil (2000), The Mid-Pleistocene climate transition as documented in the deep South Atlantic Ocean: initiation, interim state and terminal event, *Earth Planet. Sci. Lett.*, *179*, 539–549, doi:10.1016/S0012-821X(00)00143-6.

Stickley, C. E., H. Brinkhuis, S. a. Schellenberg, A. Sluijs, U. Röhl, M. Fuller, M. Grauert, M. Huber, J. Warnaar, and G. L. Williams (2004), Timing and nature of the deepening of the Tasmanian Gateway, *Paleoceanography*, *19*, PA4027, doi:10.1029/2004PA001022.

Stolz, J. F., S. B. R. Chang, and J. L. Kirschvink (1986), Magnetotactic bacteria and single-domain magnetite in hemipelagic sediments, *Nature*, *321*, 849–851, doi:10.1038/321849a0.

Suganuma, Y., T. Yamazaki, and T. Kanamatsu (2009), South Asian monsoon variability during the past 800 kyr revealed by rock magnetic proxies, *Quat. Sci. Rev.*, *28*, 926–938, doi:10.1016/j.quascirev.2008.12.014.

Sugiura N. (1979), ARM, TRM and magnetic interactions: concentration dependence, *Earth Planet. Sci. Lett*, *42*, 451-455.

Terashima, S., N. Imai, M. Taniguchi, T. Okai, and A. Nishimura (1999), The Preparation and Preliminary Characterisation of Four New Geological Survey of Japan Geochemical Reference Materials: Soils , JSO-1 and JSO-2; and Marine Sediments , JMS-1 and JMS-2, Geostt Newslett., *26*, 85–94.

Thompson, R., and F. Oldfield (1986), *Environmental Magnetism*, 227 pp., Allen and Unwin, Winchester, Mass., doi:10.1007/978-94-011-8036-8.

Verosub, K. L., and A. P. Roberts (1995) Environmental magnetism: Past, present, and future, *J. Geophys. Res.*, *100*, 2175–2192, doi:10.1029/94JB02713.

Verwey, E. J.W. (1939), Electronic conduction of magnetite（Fe_3O_4） and its transition point at low temperatures, *Nature*, *44*, 327-328.

Watkins, S. J., B. A. Maher, and G. R. Bigg (2007), Ocean circulation at the Last Glacial Maximum: A combined modeling and magnetic proxy-based study, *Paleoceanography*, *22*, PA2204, doi:10.1029/2006PA001281.

Winfrey, E. C., Doyle,P. S., Riedel, W. R. (1987), Initial Reports of the Deep Sea Drilling Project, 91, *Initial Reports of the Deep Sea Drilling Project*, U.S. Government Printing Office., *16*, 19–22.

Yamazaki, T. (2008), Magnetostatic interactions in deep-sea sediments inferred from first-order reversal curve diagrams: Implications for relative paleointensity normalization, *Geochemistry, Geophys. Geosystems*, *9*(2), doi:10.1029/2007GC001797.

Yamazaki, T. (2009), Environmental magnetism of Pleistocene sediments in the North Pacific and Ontong-Java Plateau: Temporal variations of detrital and biogenic components, *Geochemistry, Geophys. Geosystems*, *10*, Q07Z04, doi:10.1029/2009GC002413.

Yamazaki, T. (2011), Paleoposition of the Intertropical Convergence Zone in the eastern Pacific inferred from glacial-interglacial changes in terrigenous and biogenic magnetic mineral fractions, *Geology*, *40*, 151–154, doi:10.1130/G32646.1.

Yamazaki, T. (2012), Paleoposition of Intertropical Convergence Zone in the eastern Pacific inferred from glacial-interglacial changes in terrigenous and biogenic magnetic mineral fractions, *Geology*, *40*, 151–154, doi:10.1130/G32646.1.

Yamazaki and Ioka (1997), Environmental rock-magnetism of pelagic clay: Implication for Asian eolian input to the North Pacific since the Pliocene, *Paleoceanography*, *12*, 111-124.

Yamazaki, T., and H. Kawahata (1998), Organic carbon flux controls the morphology of magnetofossils in marine sediments, *Geology*, *26*, 1064-1066, doi:10.1130/0091-7613(1998)026<1064:OCFCTM>2.3.CO;2.

Yamazaki, T., and M. Ikehara (2012), Origin of magnetic mineral concentration variation in the Southern Ocean, *Paleoceanography*, *27*, PA2206, doi:10.1029/2011PA002271.

Yamazaki, T. and T. Shimono (2013), Abundant bacterial magnetite occurrence in oxic red clay, *Geology*, *41*, 1191-1194, doi:10.1130/G34782.1.

Yamazaki, T., S. Inoue, T. Shimono, T. Sakamoto, and S. Sakai (2013), Sea-ice conditions in the Okhotsk Sea during the last 550 kyr deduced from environmental magnetism, *Geochemistry, Geophys. Geosystems*, *14*, 5026–5040, doi:10.1002/2013GC004959.

Yamazaki, T., Y. Usui, and T. Shimono (2014), Magnetic properties of REY rich red clay near Minami-Torishima in the Pacific Ocean, *Japan Geoscience Union Meeting 2014*, *Abstract*, SEM37-06.

Zachos, J., M. Pagani, L. Sloan, E. Thomas, and K. Billups (2001), Trends, rhythms, and aberrations in global climate 65 Ma to present., *Science*, *292*, 686–93, doi:10.1126/science.1059412.

Zhou, L., and F. T. Kyte (1992), Sedimentation history of the South Pacific pelagic clay province over the last 85 million years inferred from the geochemistry of Deep Sea drilling Project Hole 596, *Paleoceanography*, *7*, 441–465.

Figure captions

Figure 1-1. Distribution of various lithologies of deep-sea sediments after Brown et al. (1989).

Figure 2-1. Location of Integrated Ocean Drilling Program Site U1365.

Figure 2-2. Surface chlorophyll-*a* concentrations (average between September 1997 and August 2000) in the Pacific Ocean, reflecting ocean primary productivity (Behrenfeld and Falkowski, 1997).

Figure 2-3. Paleopositions of Site U1365 since 100 Ma superimposed on a South Pacific bathymetric map. Modified after Expedition 329 Scientists (2011). Red lines are spreading centers, and white lines are isochrons.

Figure 2-4. Lithologic summary and estimated ages of Site U1365 after Expedition 329 Scientists, 2011.

Figure 2-5. Dissolved oxygen concentration of interstitial water at Site U1365 (Expedition 329 Scientists, 2011). Red squares: Hole U1365A, gray squares: Hole U1365B.

Figure 4-1. Age model above 6 mbsf at Site U1365 based on magnetostratigraphy. (a) Declination, (b) inclination, and (c) correlation to the geomagnetic polarity time scale of

Gradstein et al. (2004). Gray squares: onboard measurements after alternating-field demagnetization (AFD) at 20 mT. Blue squares are characteristic remanent magnetization (ChRM) directions after post-cruise AFD, and red squares are ChRM directions after thermal demagnetization.

Figure 4-2. Stepwise alternating-field and thermal demagnetization diagrams of representative samples with stable remanent magnetization. Solid (open) circles represent projections on the horizontal (vertical) plane.

Figure 4-3. Sedimentation rates based on magnetostratigraphy above about 6 mbsf (about 5 Ma).

Figure 4-4. Examples of stepwise alternating-field and thermal demagnetizations for samples with unstable remanent magnetization. Solid (open) circles represent projections on the horizontal (vertical) plane.

Figure 4-5. Comparison of inclinations between onboard and post-cruise measurements throughout cores at Site U1365. Gray: onboard measurements after alternating-field demagnetization (AFD) at 20 mT. Red squares: characteristic remanent magnetization (ChRM) after AFD. Blue squares: ChRM after thermal remanent magnetization.

Figure 4-6. Variations of magnetic susceptibility with depth at Site U1365 (Expedition 329 Scientists, 2011).

Figure 4-7. Inter-core correlations between IODP Site U1365 and DSDP Site 596 using magnetic susceptibility and ΣREY variation patterns. The ages of Site 596 are based on the constant Cobalt flux model of Zhou and Kyte (1992). Black: magnetic susceptibility, blue: ΣREY.

Figure 4-8. Agreement of magnetic susceptibility (upper panel) and ΣREY (lower panel) variations with age after inter-core correlation shown in Figure 4-7. Blue: Site U1365, red: Site 596.

Figures 4-9. Examples of high-resolution first-order reversal curve (FORC) diagrams and coercivity profiles along the *H*c axis at Hu = 0. All diagrams have sharp ridges along the coercivity axis, which are indicative of noninteracting single-domain grains of bacterial origin.

Figure 4-10. An example of low-resolution FORC diagrams.

Figure 4-11. Variations of k_{ARM}/SIRM (ratio of anhysteretic remanent magnetization susceptibility to saturation isothermal remanent magnetization) with depth. High values suggest dominance of biogenic magnetite.

Figure 4-12. Examples of FORC diagrams and results of isothermal remanent magnetization (IRM) component analyses: (a) FORC diagrams, and (b) IRM components. Squares represent data points that define gradient of IRM acquisition curves, which can be described by sum (black

curve) of low-coercivity (L, red curve), middle-coercivity (M, green curve), and very low coercivity (VL, blue curve) components; L component is considered to represent biogenic magnetite.

Figure 4-13. Variations of S ratios, $S_{-0.1T}$ and $S_{-0.3T}$, with depth. Left panel: $S_{-0.1T}$, right panel: $S_{-0.3T}$.

Figures 4-14. Examples of low-temperature magnetic measurements. Upper panels: low-temperature cycling of room-temperature SIRM (blue: cooling, red: heating). Lower panels: thermal demagnetization curves of SIRM acquired at 6 K.

Figure 4-15. Variations of magnetization with temperature from room temperature to 700 ºC. Red: heating, blue: cooling.

Figures 4-16. Transmission electron microscope images of magnetic extracts from red clay at 10.14 mbsf of Site U1365.

Figure 5-1. Summary of magnetic property changes with age. (a) k_{ARM}/SIRM ratio, (b) FORC diagrams, and (c) IRM components. See Figure 4-12 for colors of IRM components.

Figure 5-2. Summary of temporal variations in rock-magnetic properties, ΣREY content, and sedimentation rates. (a) magnetic susceptibility, (b) ΣREY content, (c) k_{ARM}/SIRM ratio, (d) proportion of M component in IRM component analyses, and (e) sedimentation rate.

Figure 5-3. Movement of Site U1365 and Australia with age, and seafloor ages. The Gplates software (Seton et al., 2012) were used.

Figure 5-4. Variations of (a) magnetic susceptibility, (b) k_{ARM}/SIRM ratio, and ΣREY content with depth for a red clay core taken near Minami-Torishima (Yamazaki et al., 2014). The location of the core is shown in panel (c).

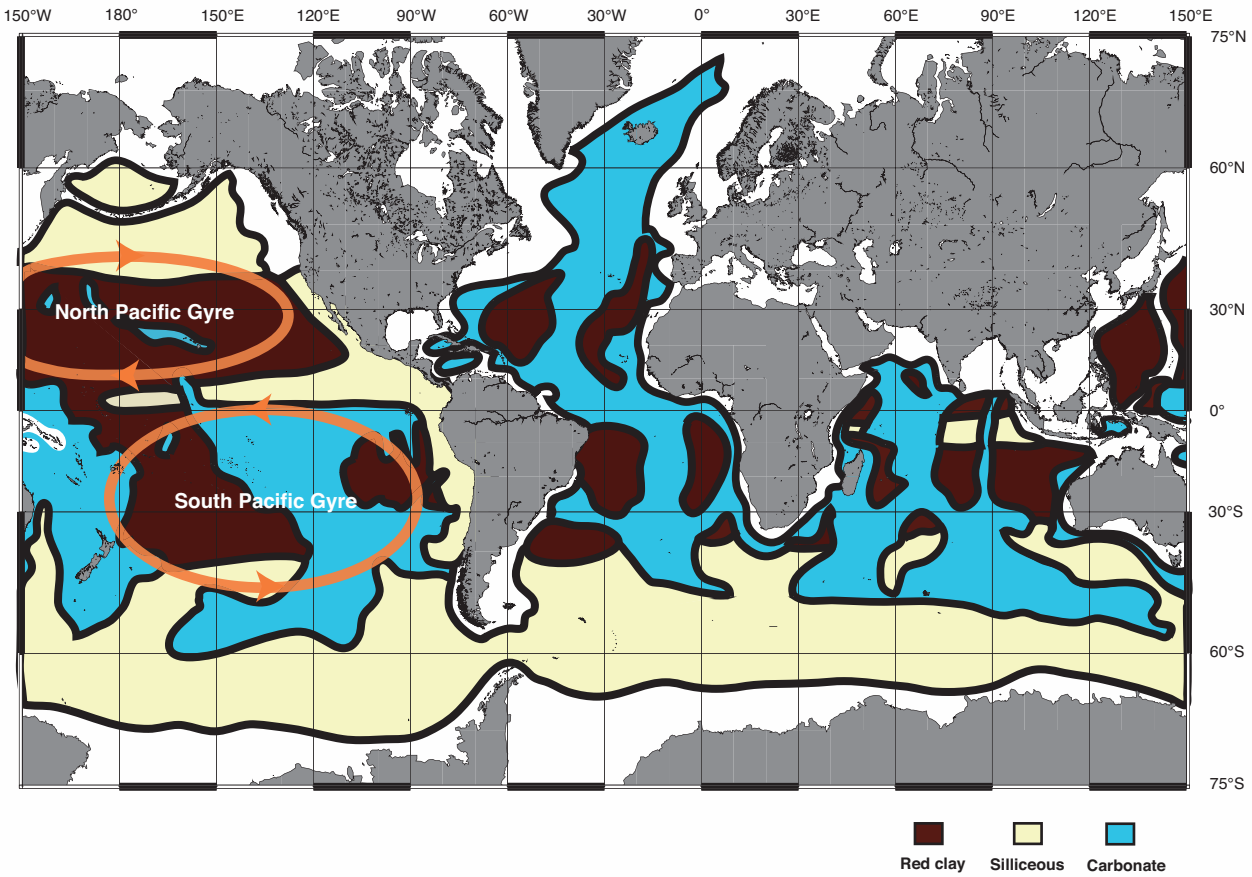
150°W
180°
150°E
120°E
90°W
60°W
30°W
0°
30°E
60°E
90°E
120°E
150°E
75°N
60°N
30°N
0°
30°S
60°S
75°S
North Pacific Gyre
South Pacific Gyre
Red clay
Silliceous
Carbonate

Figure 1-1

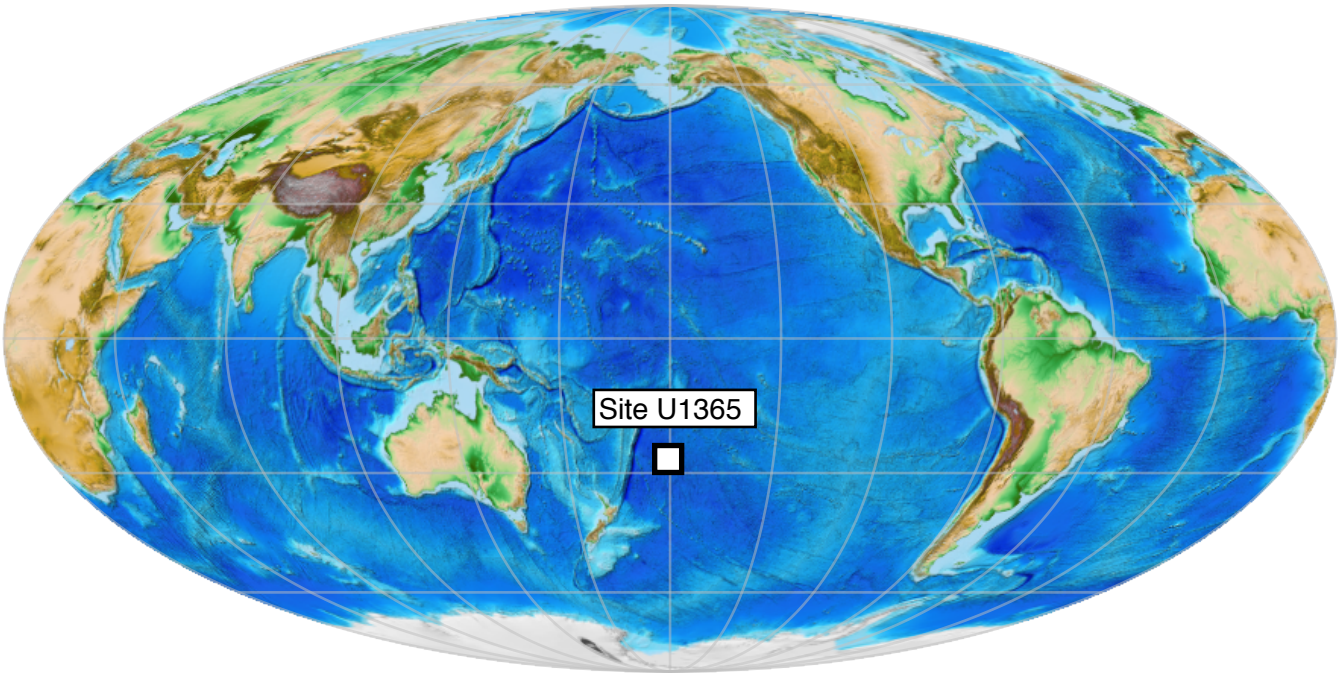

Figure 1-2

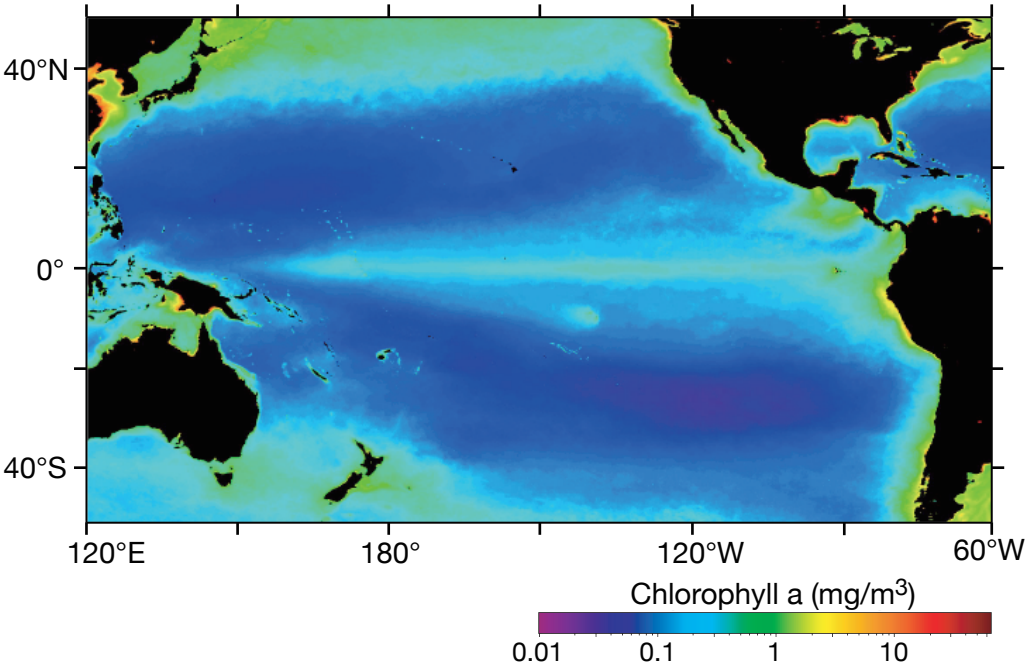

Figure 2-1

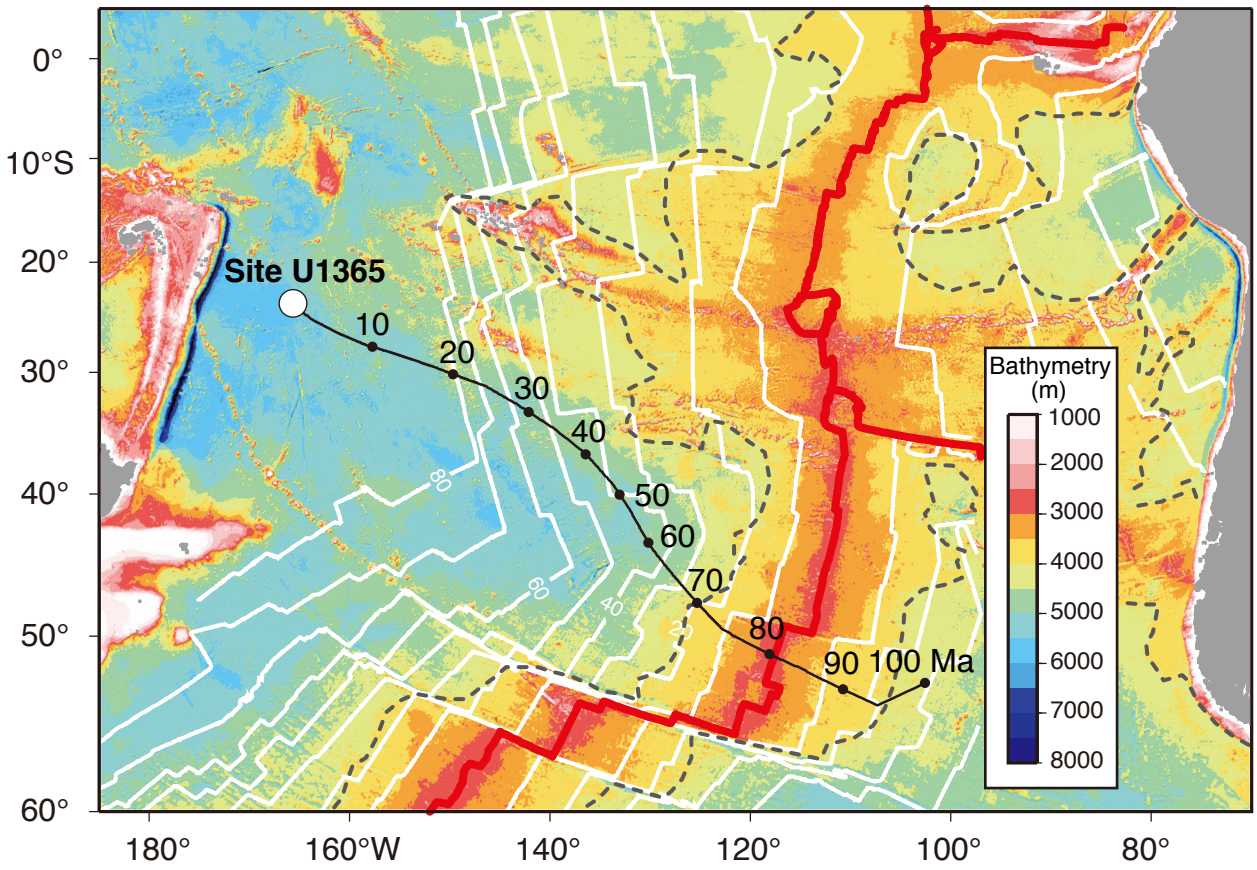
0°
10°S
20°
30°
40°
50°
60°
180°
160°W
140°
120°
100°
80°
Site U1365
10
20
30
40
50
60
70
80
90 100 Ma
Bathymetry (m)
1000
2000
3000
4000
5000
6000
7000
8000

Figure 2-2

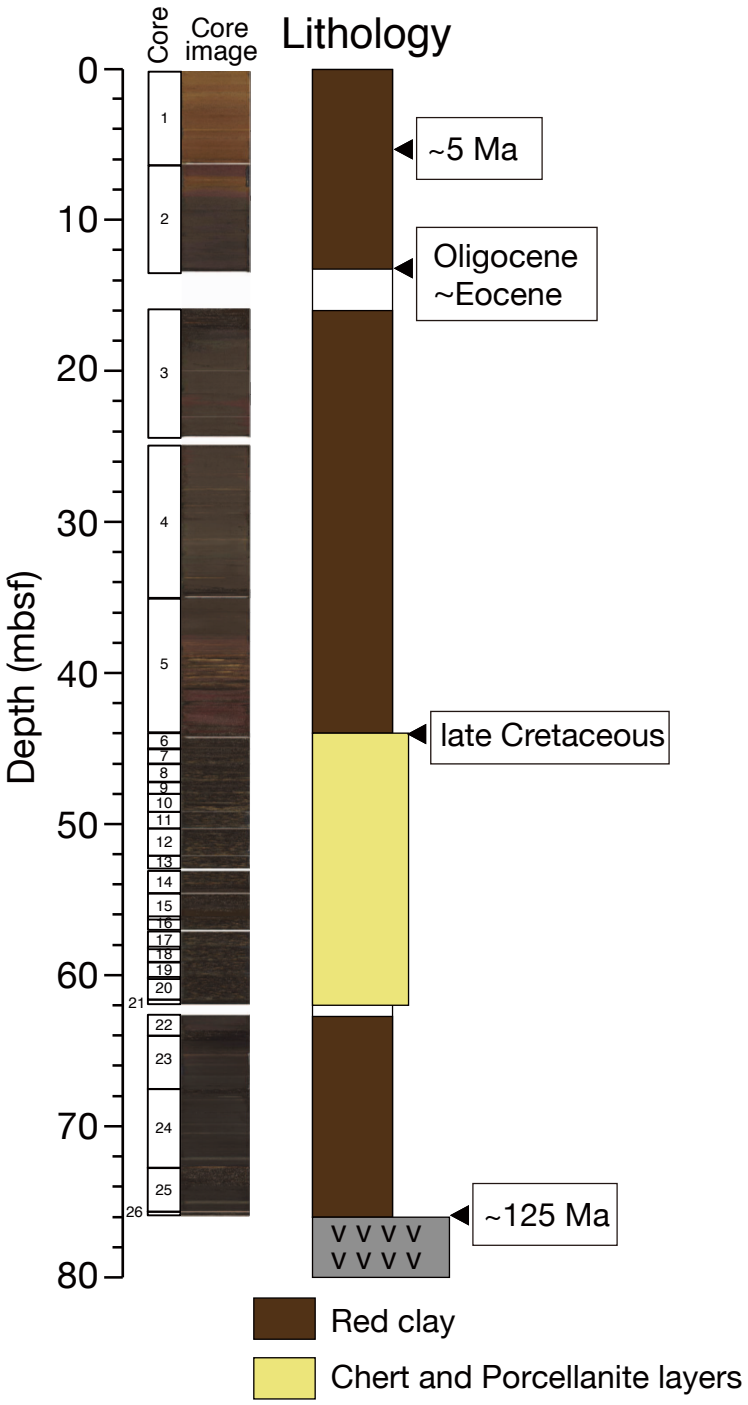
Core
Core image
Lithology
Depth (mbsf)
0
10
20
30
40
50
60
70
80
1
2
3
4
5
6
7
8
9
10
11
12
13
14
15
16
17
18
19
20
21
22
23
24
25
26
~5 Ma
Oligocene ~Eocene
late Cretaceous
~125 Ma
Red clay
Chert and Porcellanite layers

Figure 2-3

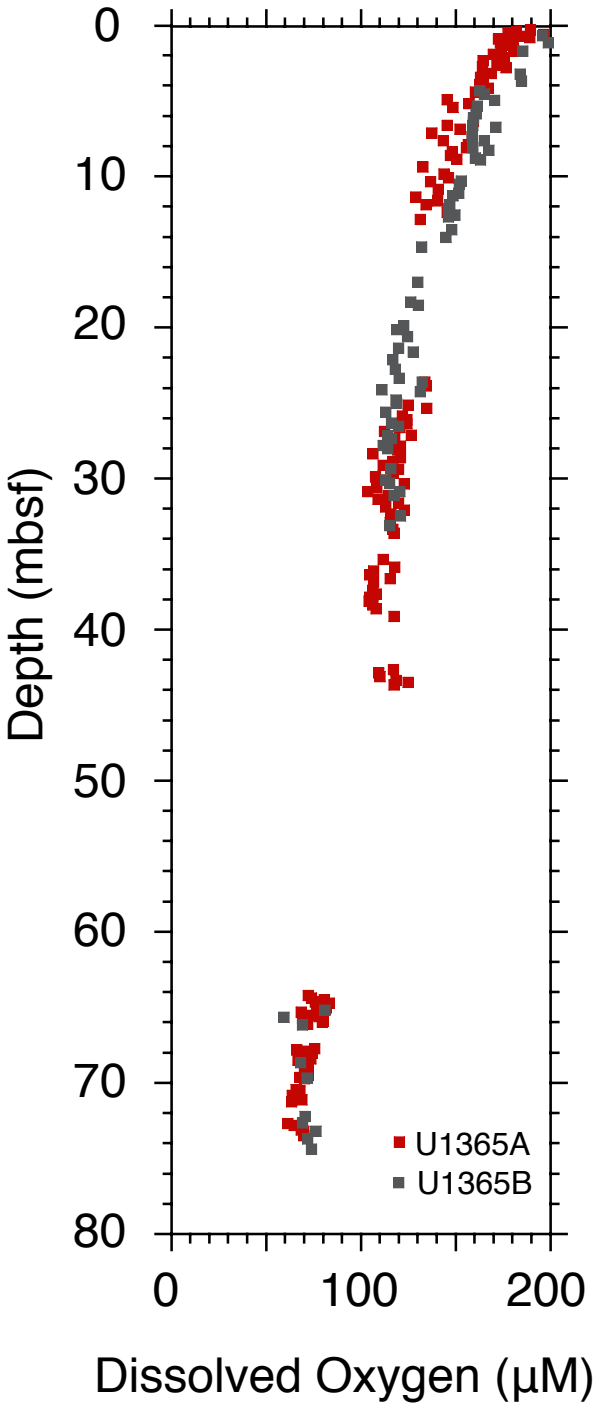
0
10
20
30
40
50
60
70
80
Depth (mbsf)
0
100
200
Dissolved Oxygen (µM)
U1365A
U1365B

Figure 2-4

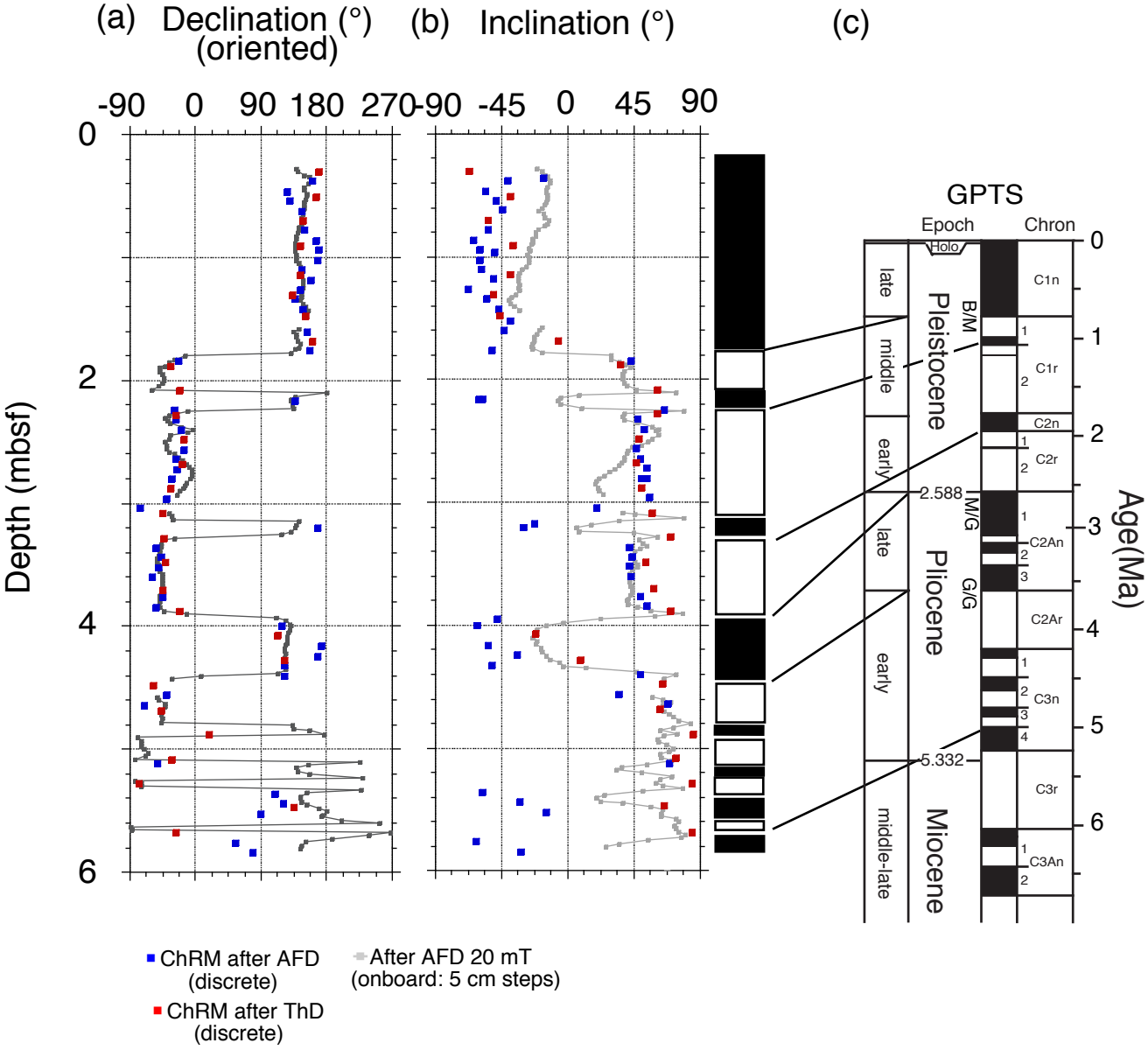
(a) Declination (°) (oriented)
(b) Inclination (°)
(c)
-90 0 90 180 270
-90 -45 0 45 90
Depth (mbsf)
0
2
4
6
GPTS
Epoch
Chron
Holo
late
middle
early
late
early
middle-late
Pleistocene
Pliocene
Miocene
B/M
M/G
G/G
2.588
5.332
C1n
C1r
C2n
C2r
C2An
C2Ar
C3n
C3r
C3An
Age(Ma)
ChRM after AFD (discrete)
ChRM after ThD (discrete)
After AFD 20 mT (onboard: 5 cm steps)

Figure 4-1

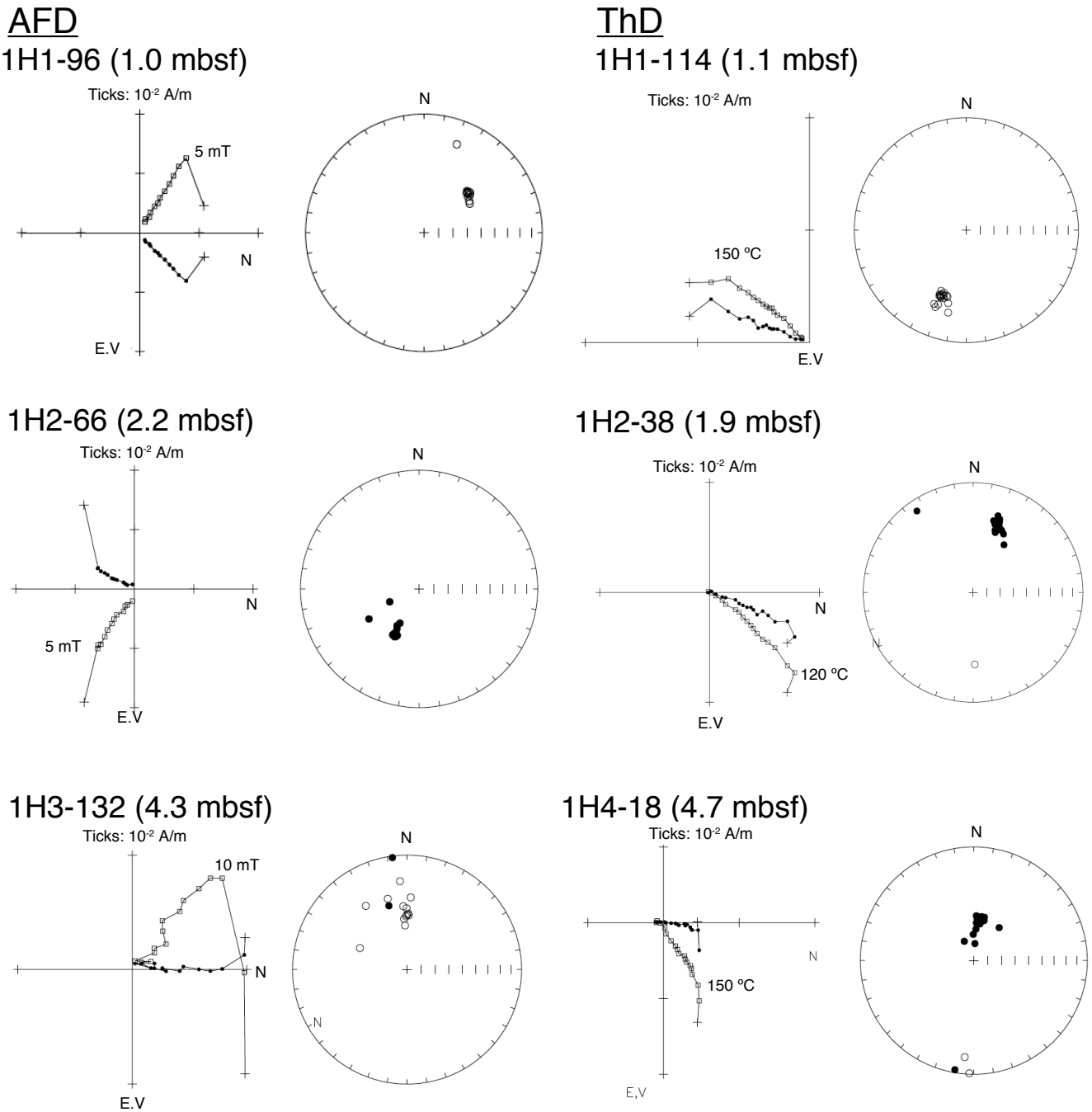
AFD
1H1-96 (1.0 mbsf)
Ticks: 10-2 A/m
5 mT
N
E.V
N
ThD
1H1-114 (1.1 mbsf)
Ticks: 10-2 A/m
150 ºC
E.V
N
1H2-66 (2.2 mbsf)
Ticks: 10-2 A/m
N
5 mT
E.V
N
1H2-38 (1.9 mbsf)
Ticks: 10-2 A/m
N
120 ºC
E.V
N
1H3-132 (4.3 mbsf)
Ticks: 10-2 A/m
10 mT
N
E.V
N
1H4-18 (4.7 mbsf)
Ticks: 10-2 A/m
N
150 ºC
E,V
N

Figure 4-2

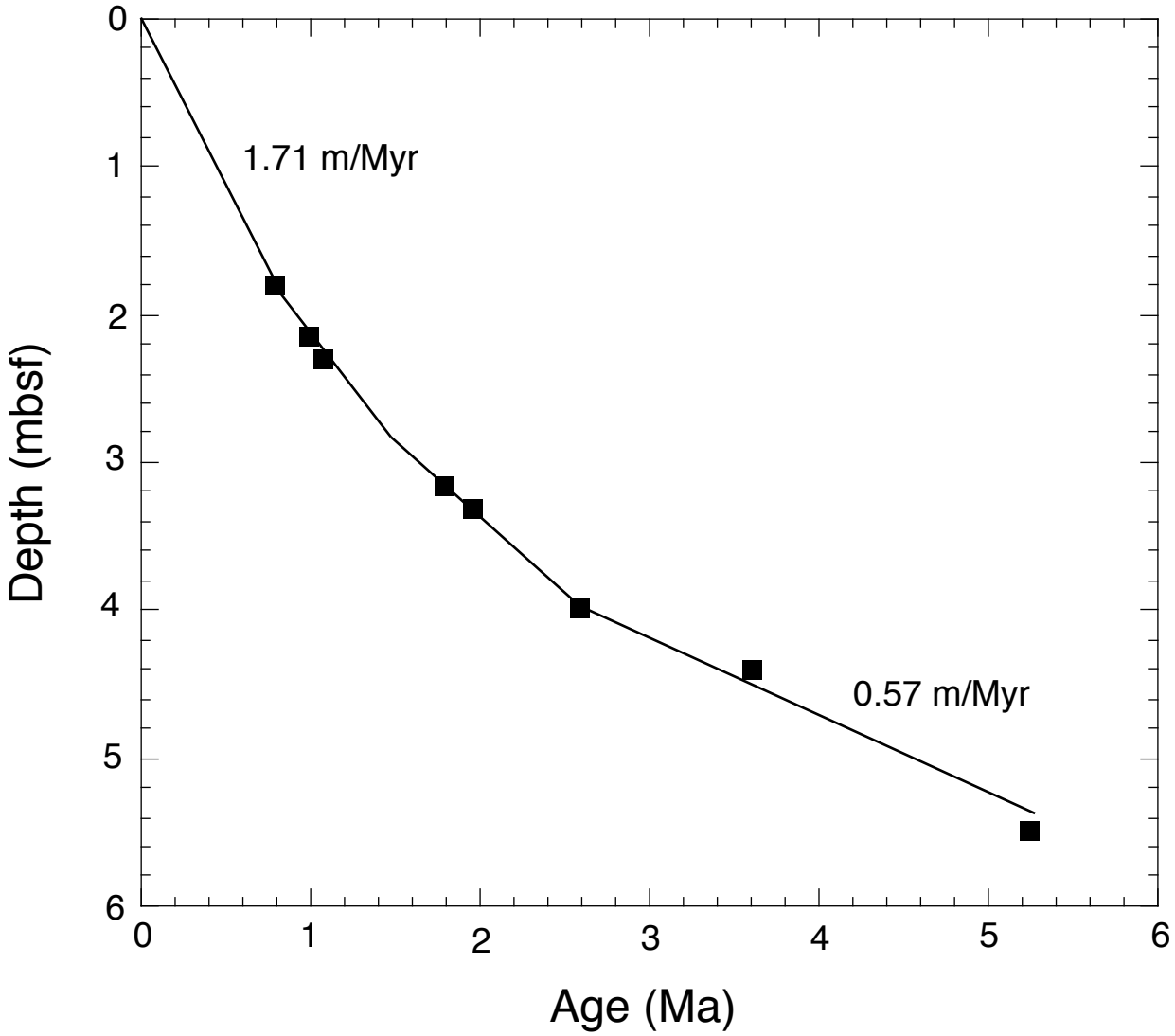

Figure 4-3

AFD

2H1-32 (6.5 mbsf)

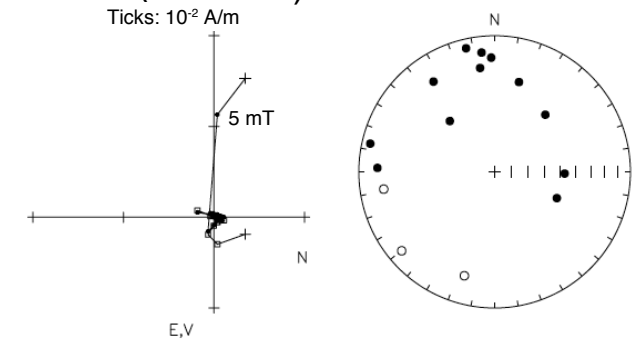

3H5-42 (21.7 mbsf)

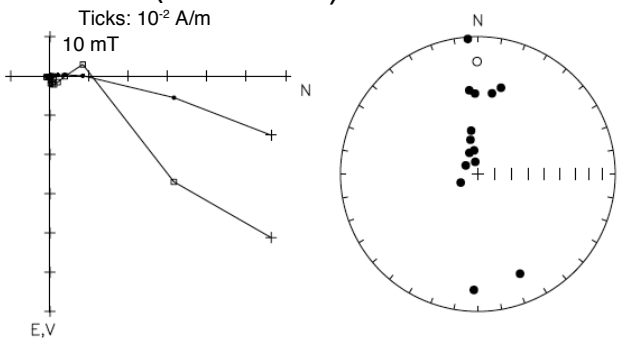

5H1-32 (35.3 mbsf)

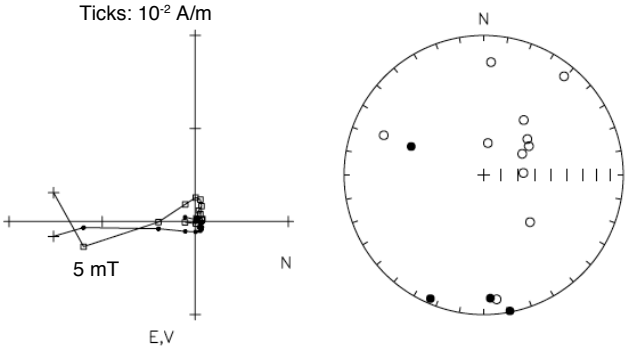

ThD

2H1-88 (7.1 mbsf)

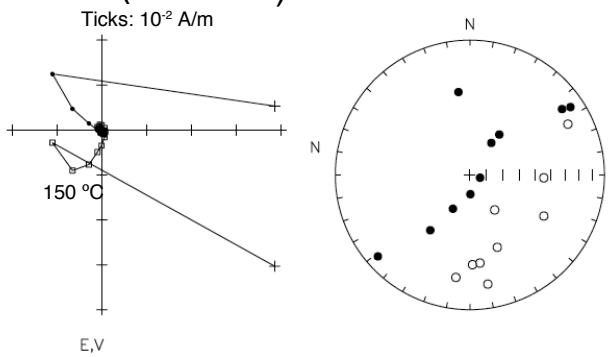

2H2-34 (8.0 mbsf)

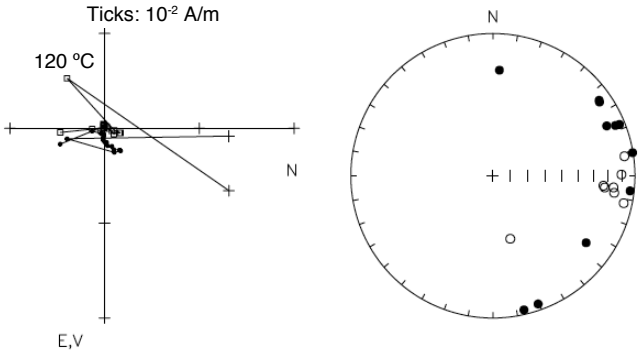

2H2-24 (9.4 mbsf)

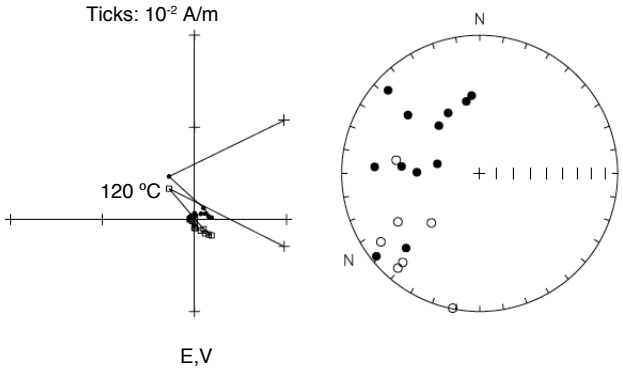

Figure 4-4

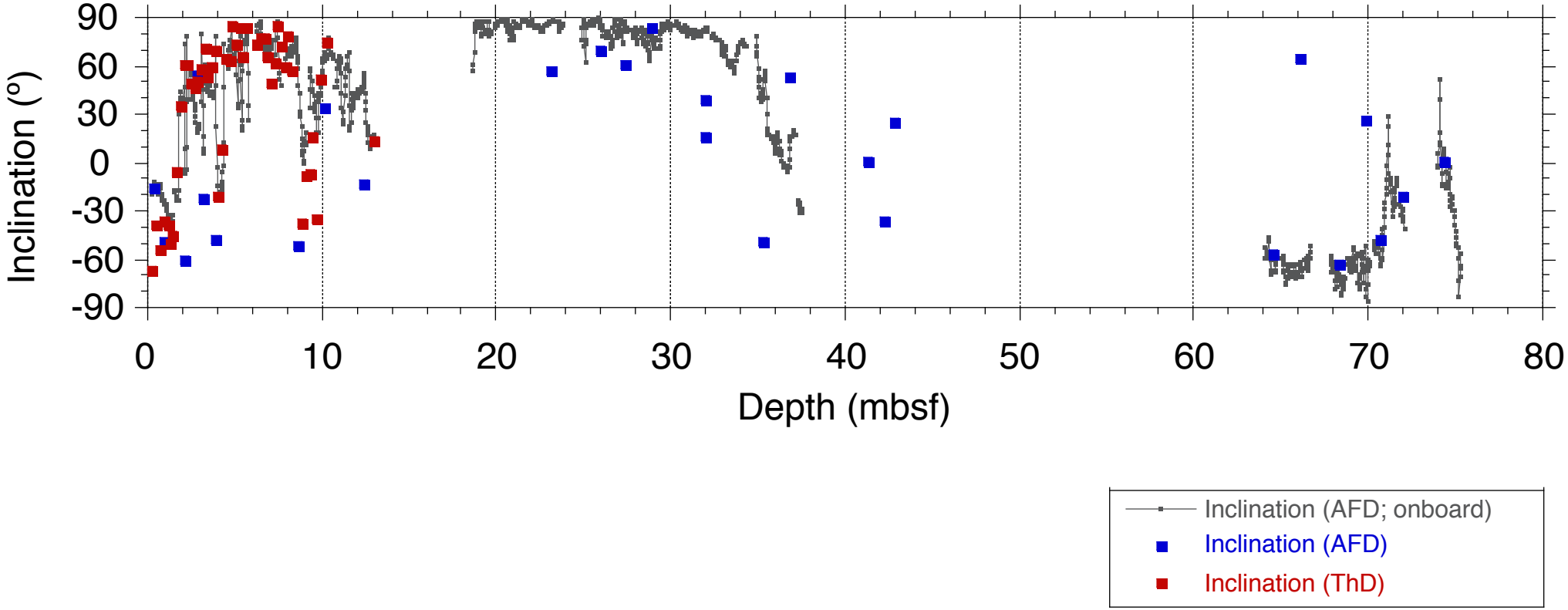
Inclination (°)
90
60
30
0
-30
-60
-90
0
10
20
30
40
50
60
70
80
Depth (mbsf)
Inclination (AFD; onboard)
Inclination (AFD)
Inclination (ThD)

Figure 4-5

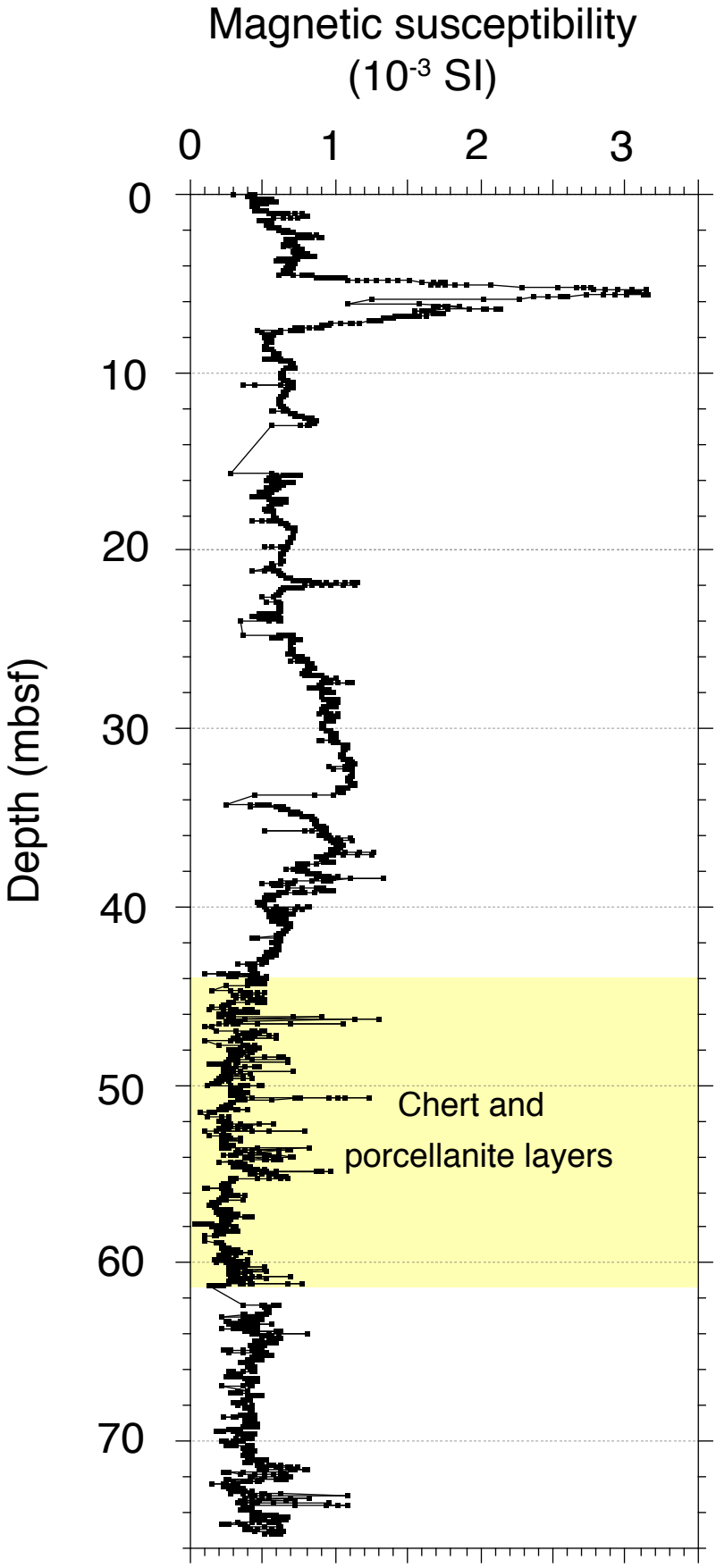
Magnetic susceptibility
(10-3 SI)
0
1
2
3
Depth (mbsf)
0
10
20
30
40
50
60
70
Chert and
porcellanite layers

Figure 4-6

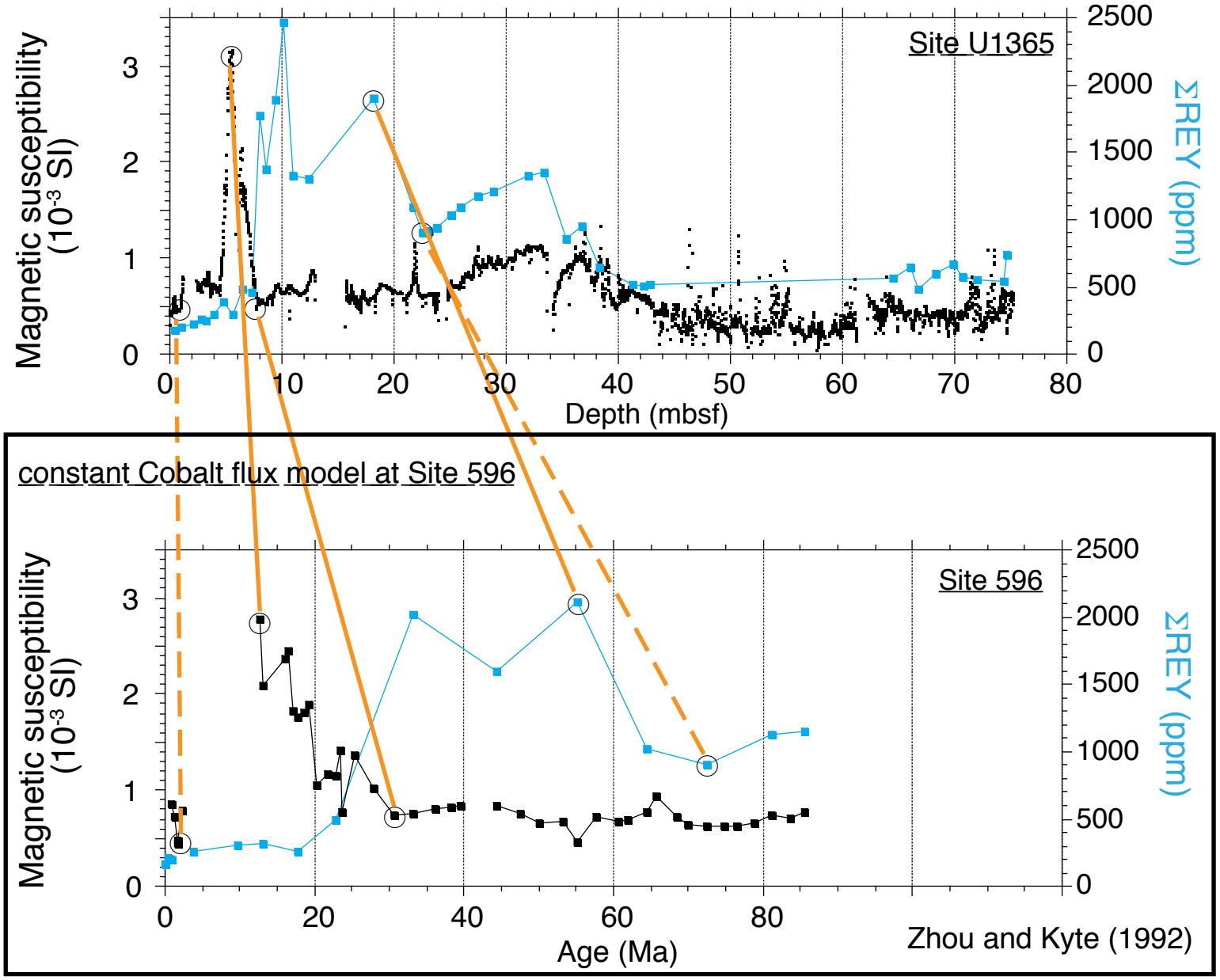
Site U1365
Magnetic susceptibility (10^{-3} SI)
ΣREY (ppm)
Depth (mbsf)
constant Cobalt flux model at Site 596
Site 596
Age (Ma)
Zhou and Kyte (1992)

Figure 4-7

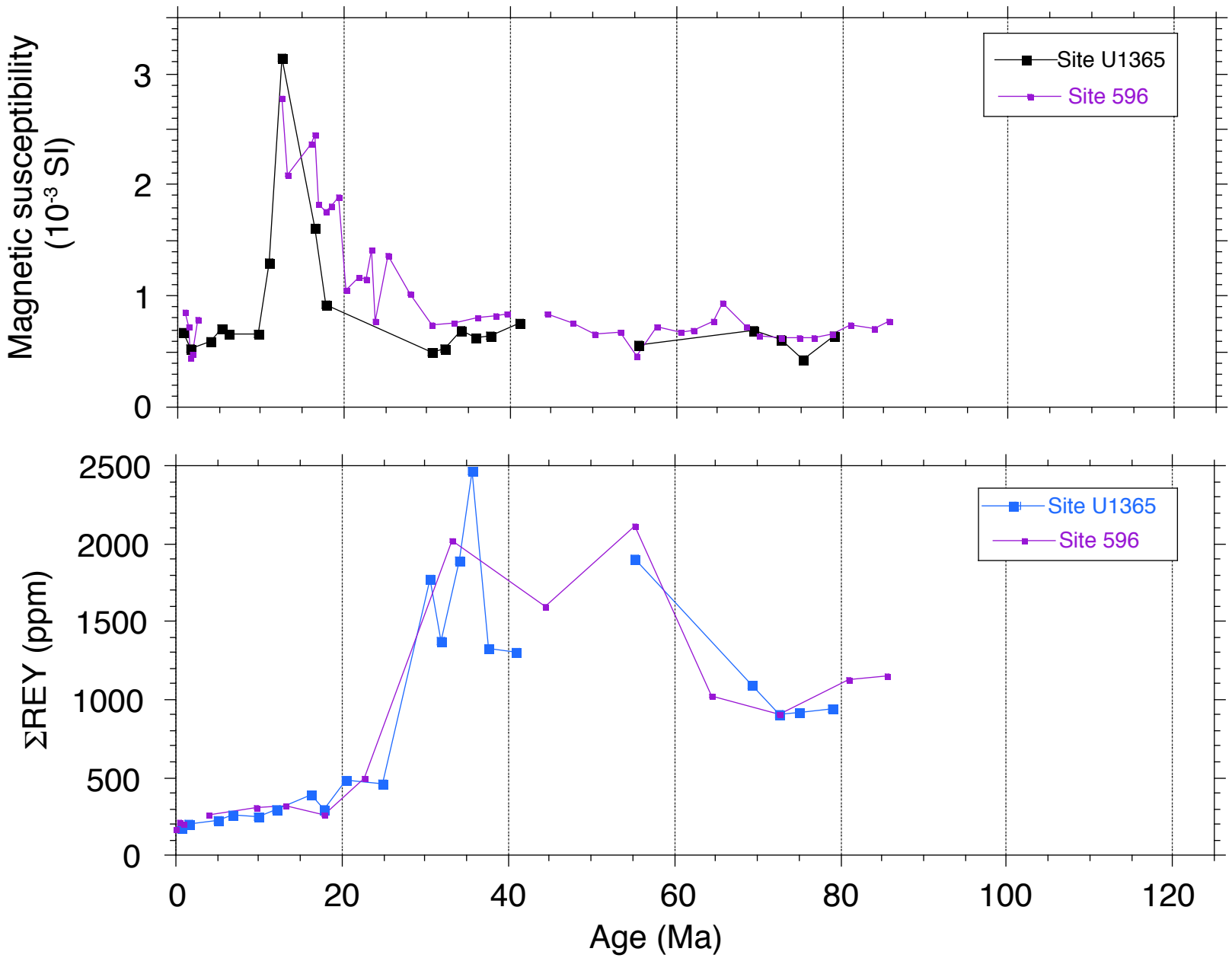
Magnetic susceptibility
(10-3 SI)
0
1
2
3
Site U1365
Site 596
ΣREY (ppm)
0
500
1000
1500
2000
2500
Site U1365
Site 596
0
20
40
60
80
100
120
Age (Ma)

Figure 4-8

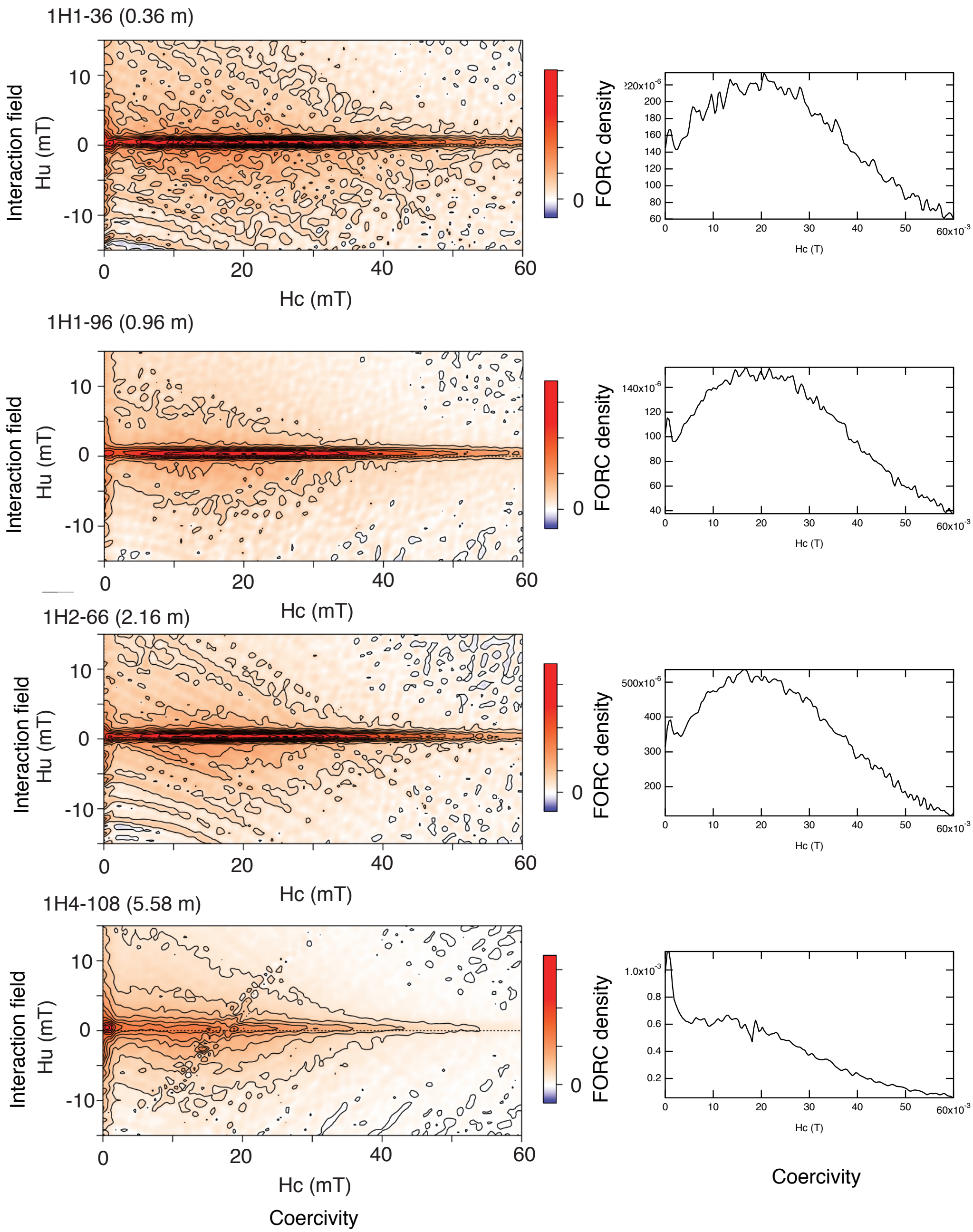
1H1-36 (0.36 m)
Interaction field
Hu (mT)
Hc (mT)
FORC density
Hc (T)
1H1-96 (0.96 m)
1H2-66 (2.16 m)
1H4-108 (5.58 m)
Coercivity

Figure 4-9

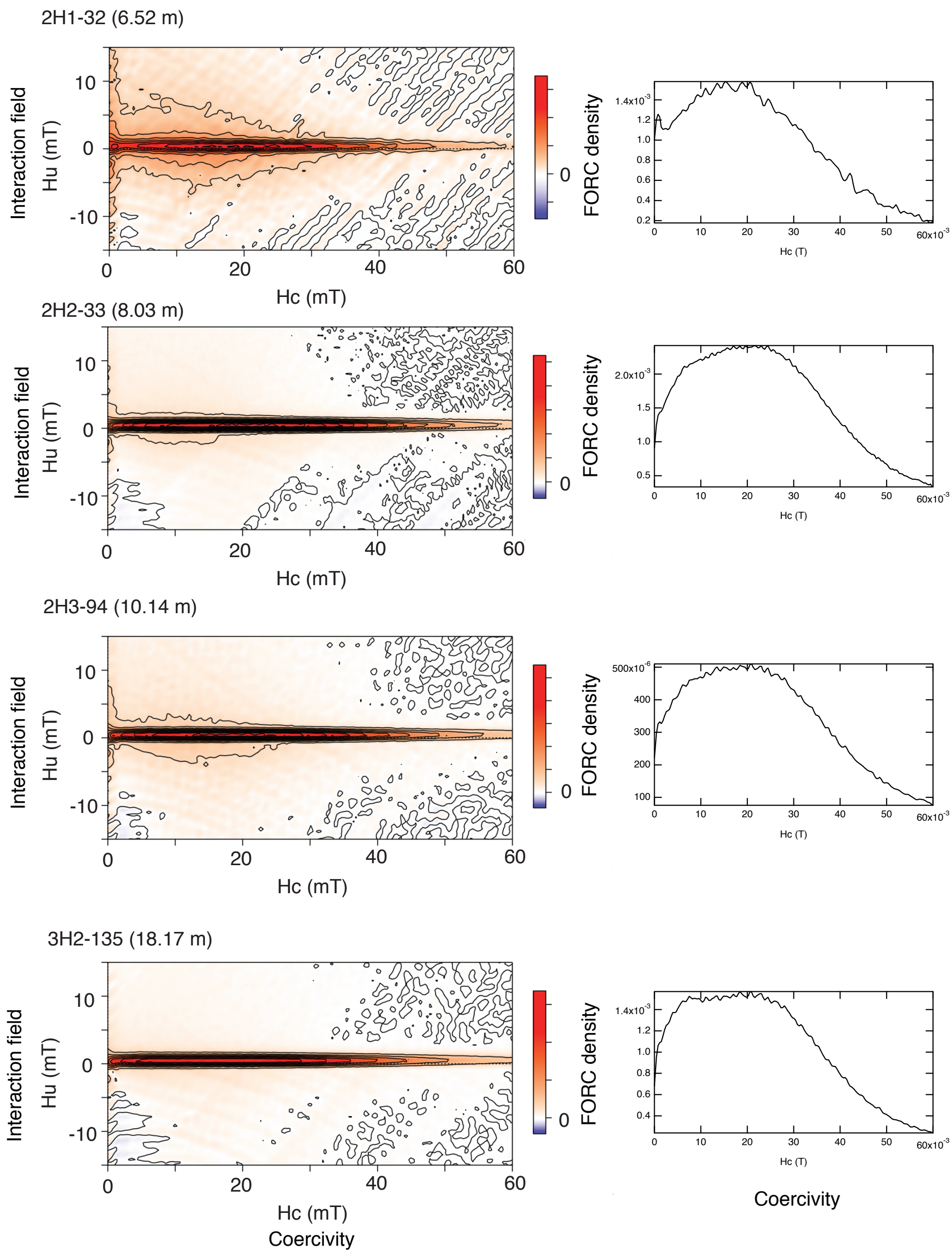

Figure 4-9 (continued)

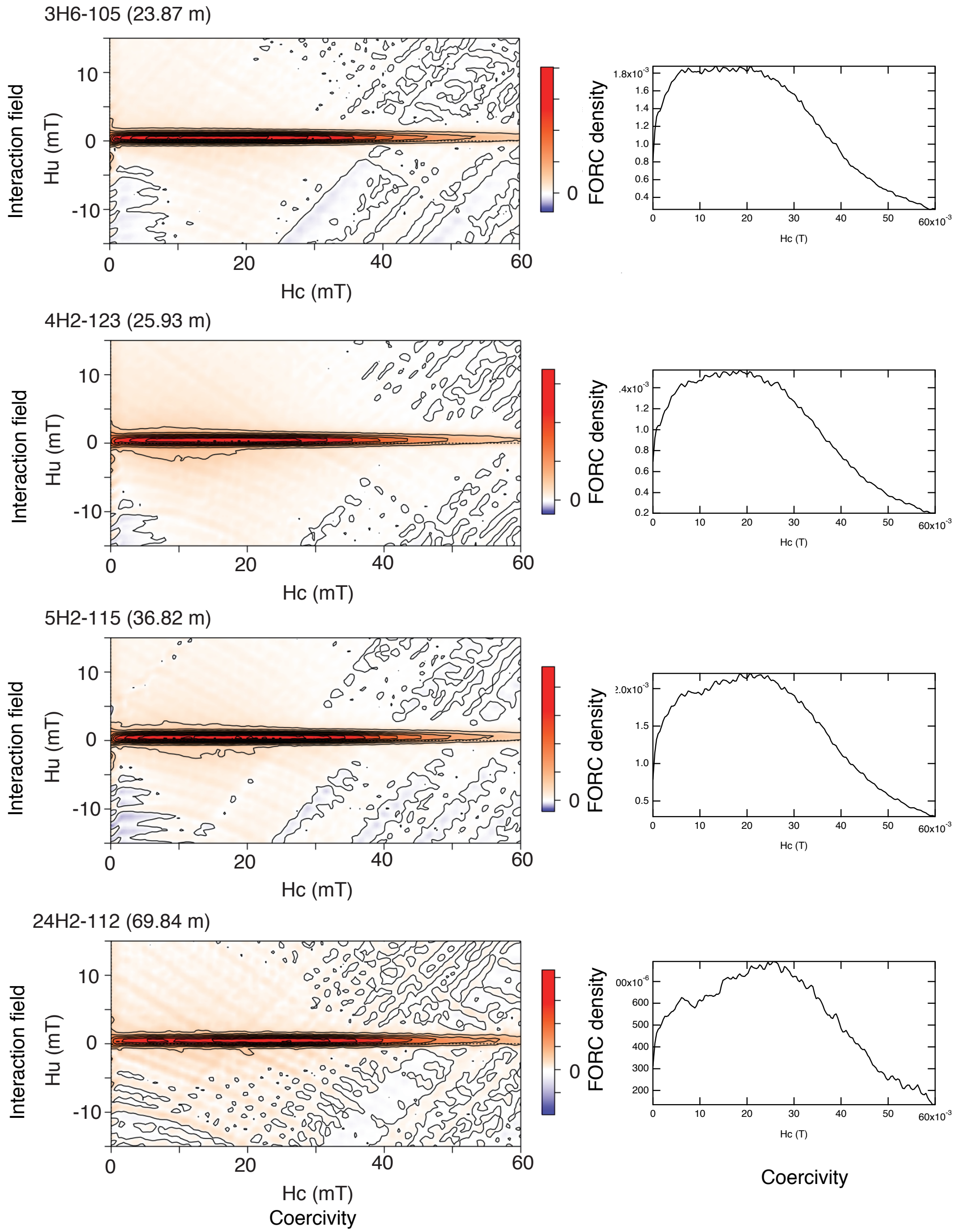

Figure 4-9 (continued)

1H2-130 (2.8 mbsf)

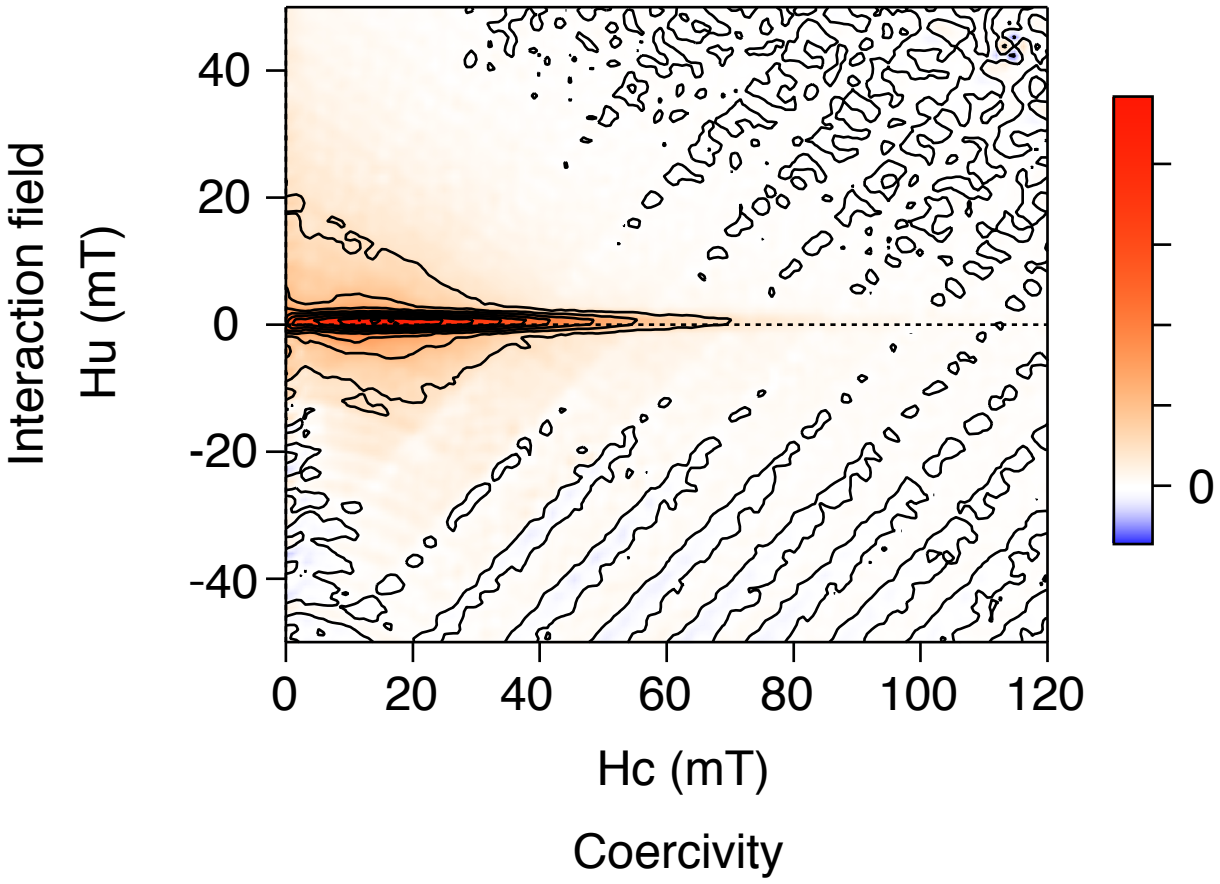

Figure 4-10

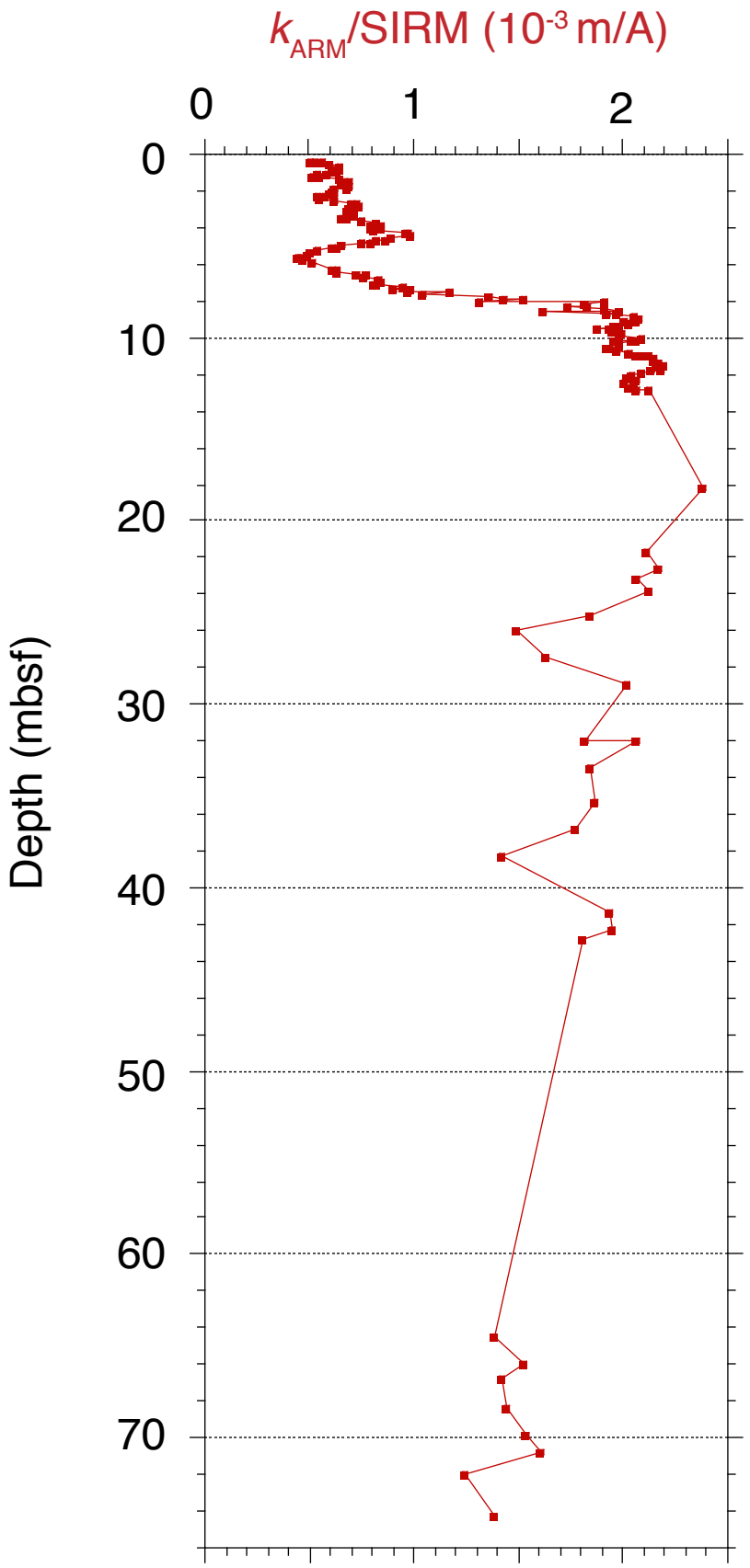

Figure 4-11

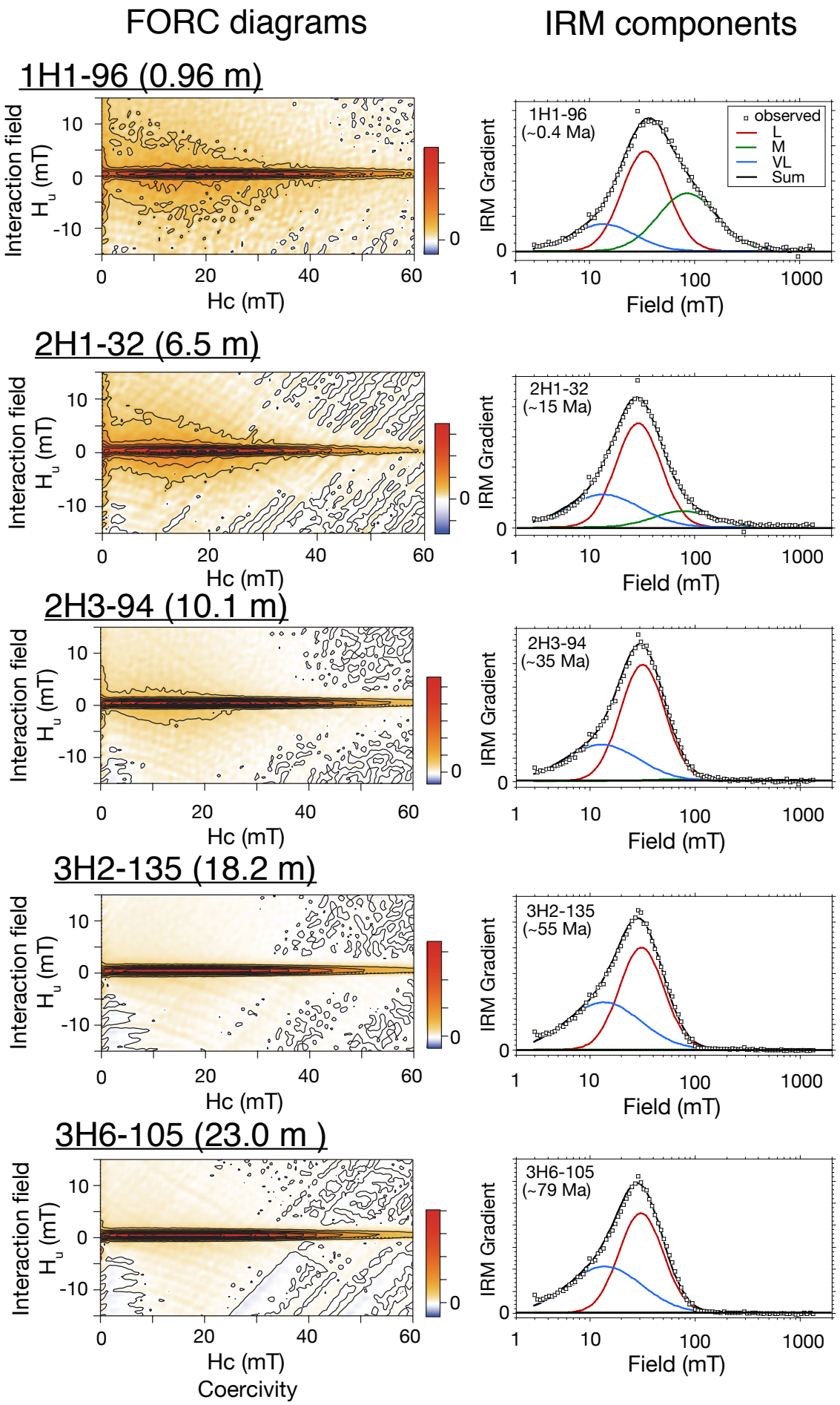
FORC diagrams
IRM components
1H1-96 (0.96 m)
2H1-32 (6.5 m)
2H3-94 (10.1 m)
3H2-135 (18.2 m)
3H6-105 (23.0 m)
Interaction field
H_u (mT)
Hc (mT)
Coercivity
IRM Gradient
Field (mT)
1H1-96
(~0.4 Ma)
2H1-32
(~15 Ma)
2H3-94
(~35 Ma)
3H2-135
(~55 Ma)
3H6-105
(~79 Ma)
observed
L
M
VL
Sum

Figure 4-12

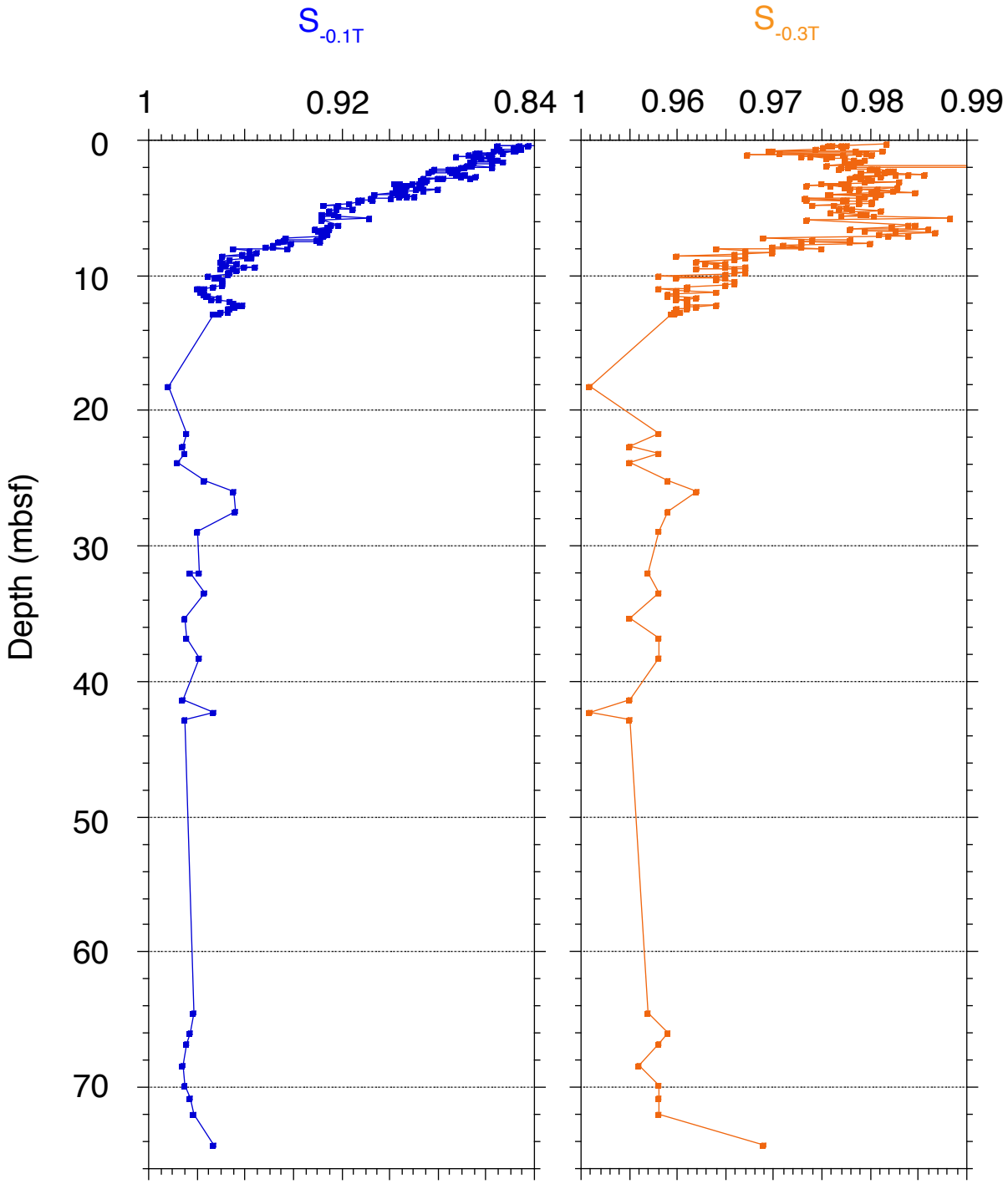
S-0.1T
S-0.3T
1
0.92
0.84
1
0.96
0.97
0.98
0.99
0
10
20
30
40
50
60
70
Depth (mbsf)

Figure 4-13

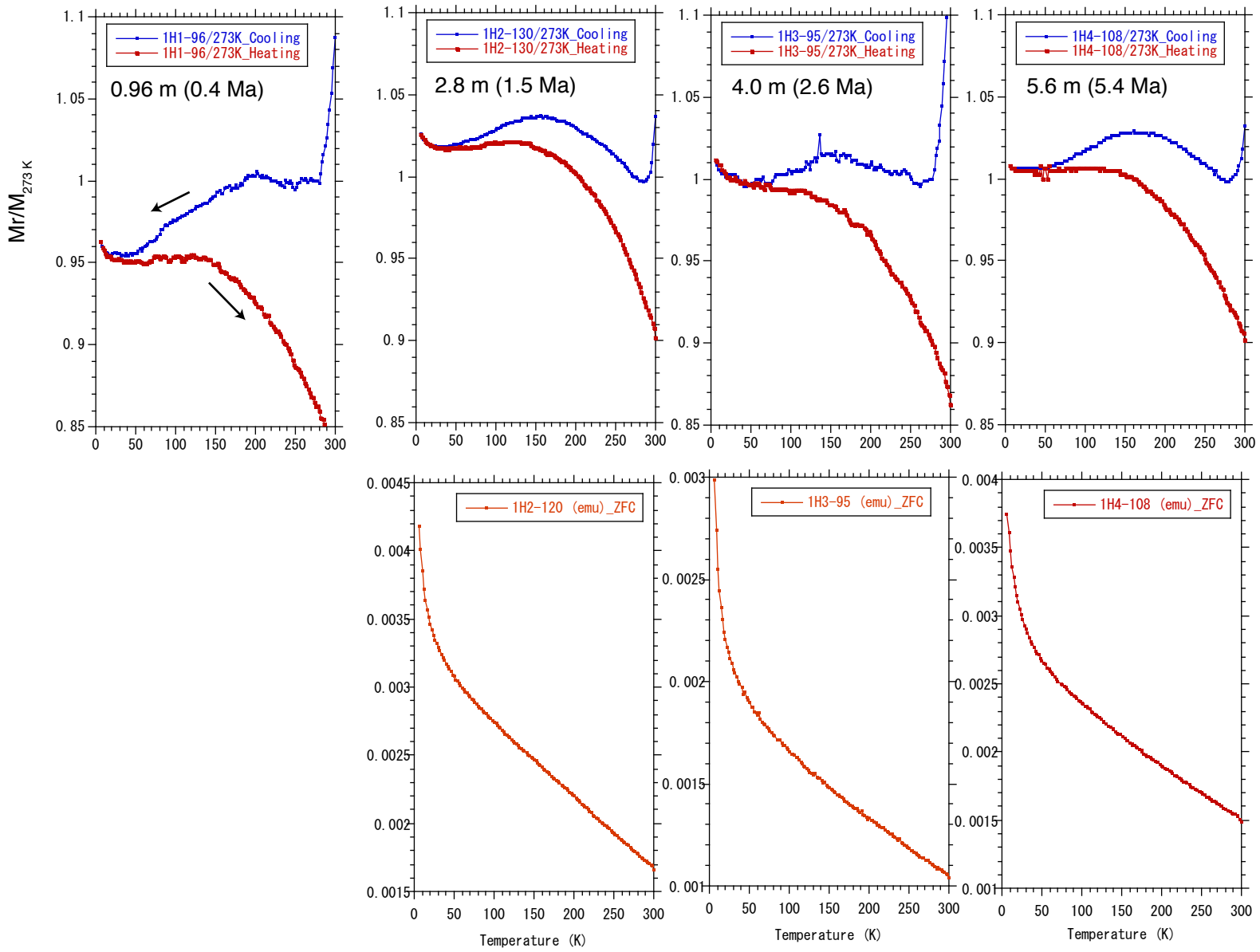
Mr/M273 K
1H1-96/273K_Cooling
1H1-96/273K_Heating
0.96 m (0.4 Ma)
1H2-130/273K_Cooling
1H2-130/273K_Heating
2.8 m (1.5 Ma)
1H3-95/273K_Cooling
1H3-95/273K_Heating
4.0 m (2.6 Ma)
1H4-108/273K_Cooling
1H4-108/273K_Heating
5.6 m (5.4 Ma)
1H2-120 (emu)_ZFC
1H3-95 (emu)_ZFC
1H4-108 (emu)_ZFC
Temperature (K)
Temperature (K)
Temperature (K)

Figure 4-14

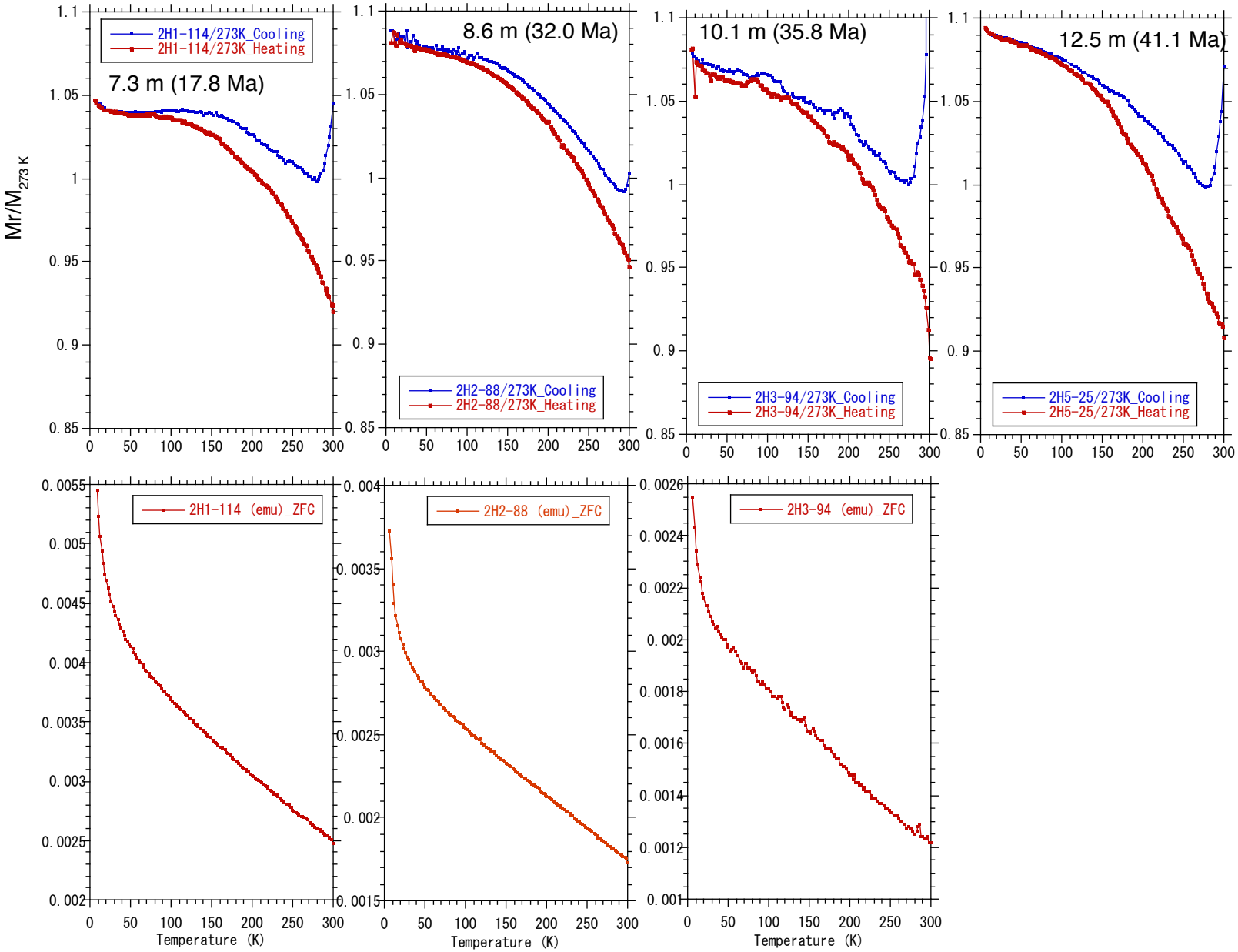

Figure 4-14 (continued)

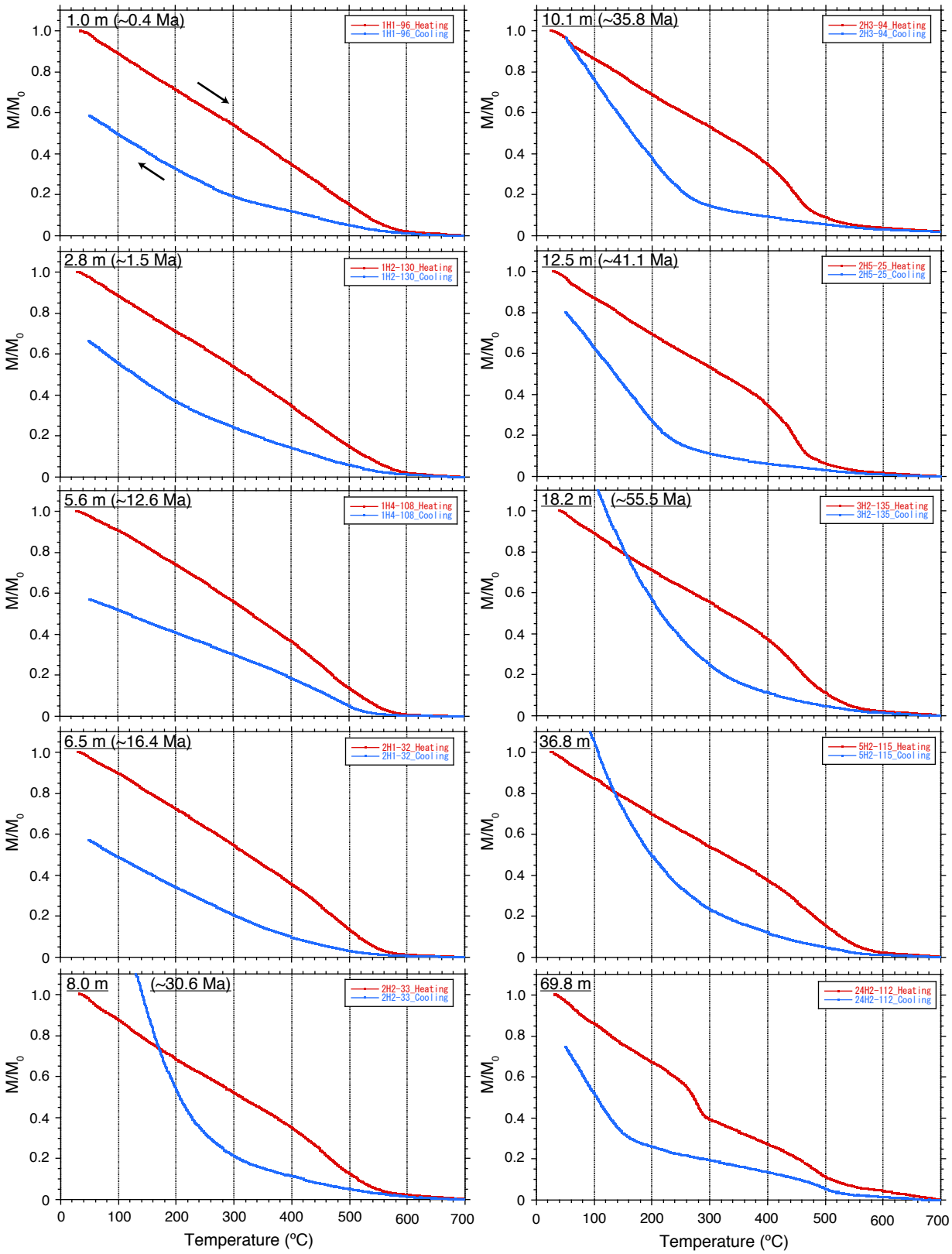
1.0 m (~0.4 Ma)
1H1-96_Heating
1H1-96_Cooling
10.1 m (~35.8 Ma)
2H3-94_Heating
2H3-94_Cooling
2.8 m (~1.5 Ma)
1H2-130_Heating
1H2-130_Cooling
12.5 m (~41.1 Ma)
2H5-25_Heating
2H5-25_Cooling
5.6 m (~12.6 Ma)
1H4-108_Heating
1H4-108_Cooling
18.2 m (~55.5 Ma)
3H2-135_Heating
3H2-135_Cooling
6.5 m (~16.4 Ma)
2H1-32_Heating
2H1-32_Cooling
36.8 m
5H2-115_Heating
5H2-115_Cooling
8.0 m (~30.6 Ma)
2H2-33_Heating
2H2-33_Cooling
69.8 m
24H2-112_Heating
24H2-112_Cooling
M/M0
Temperature (°C)

Figure 4-15

(a)

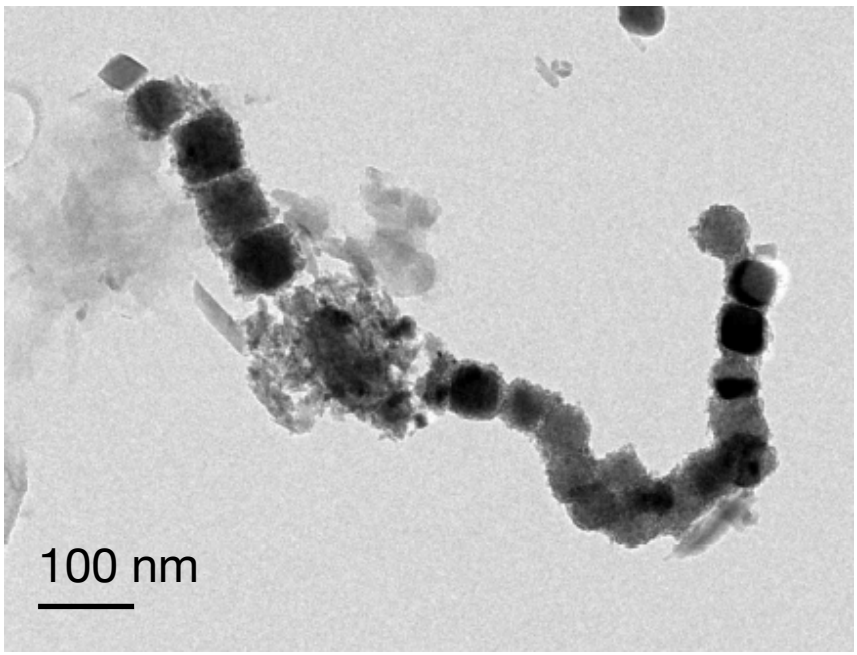

(b)

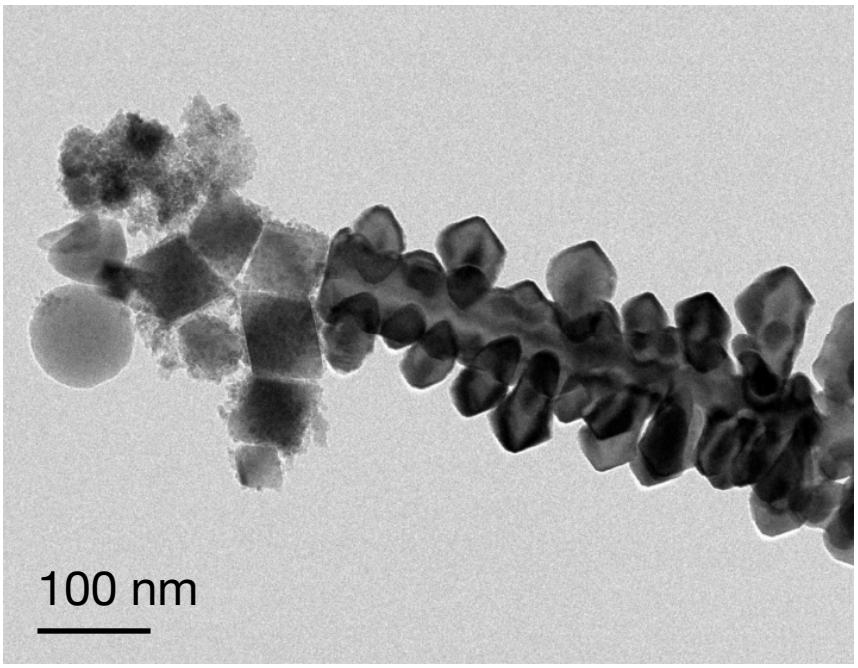

Figure 4-16

(c)

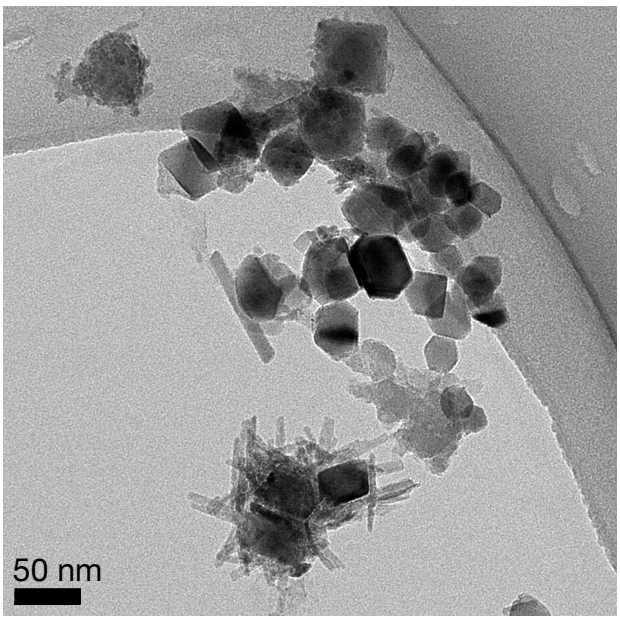

(d)

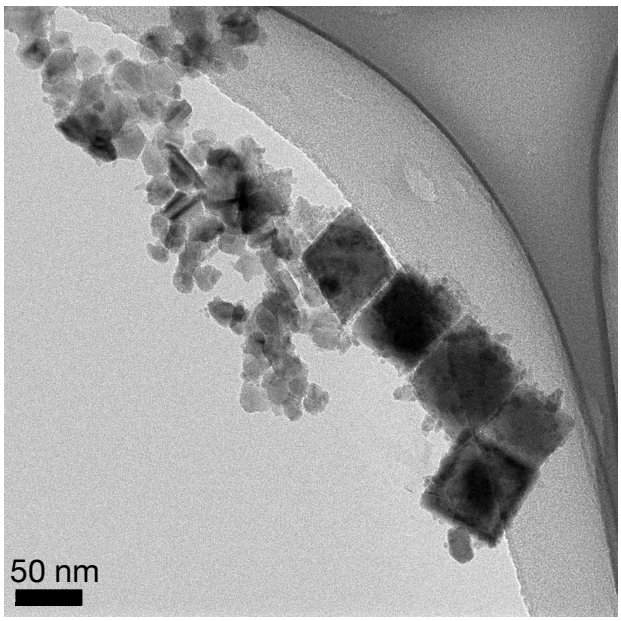

(e)

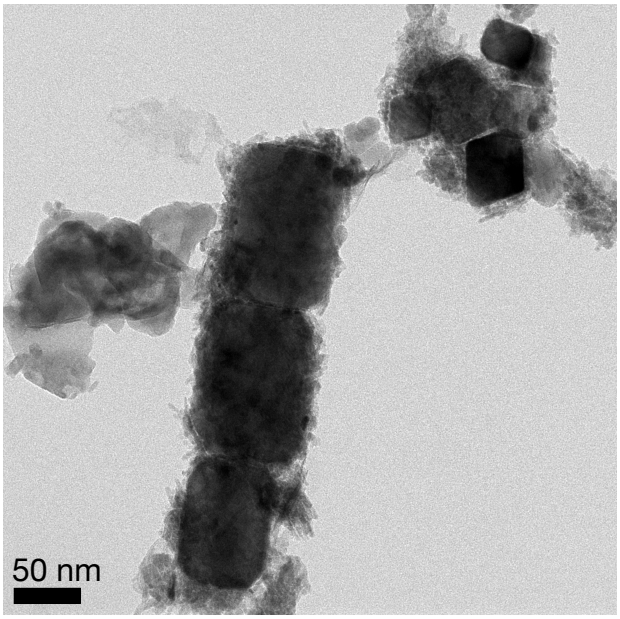

(f)

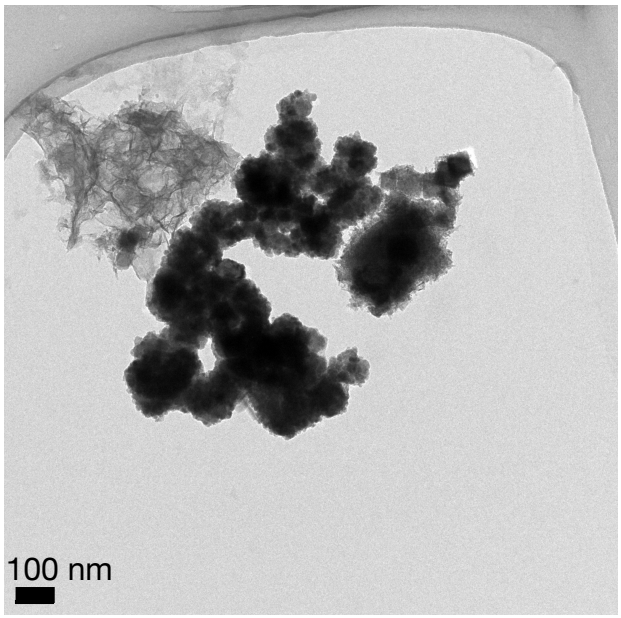

Figure 4-16 (continued)

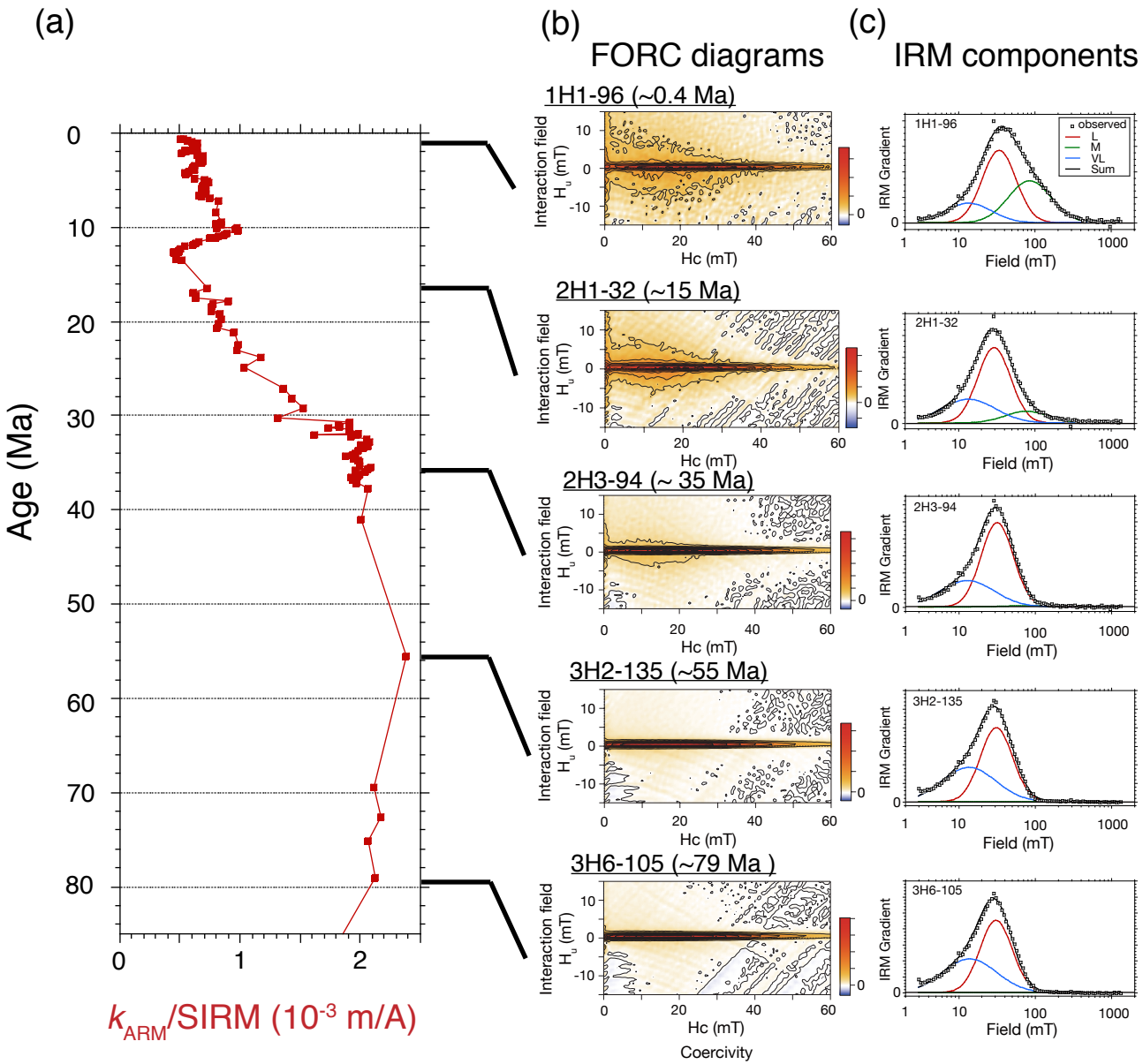
(a)
(b)
FORC diagrams
(c)
IRM components
1H1-96 (~0.4 Ma)
2H1-32 (~15 Ma)
2H3-94 (~ 35 Ma)
3H2-135 (~55 Ma)
3H6-105 (~79 Ma)
Age (Ma)
k_{ARM}/SIRM (10^{-3} m/A)
Interaction field H_u (mT)
Hc (mT)
Coercivity
IRM Gradient
Field (mT)
observed
L
M
VL
Sum

Figure 5-1

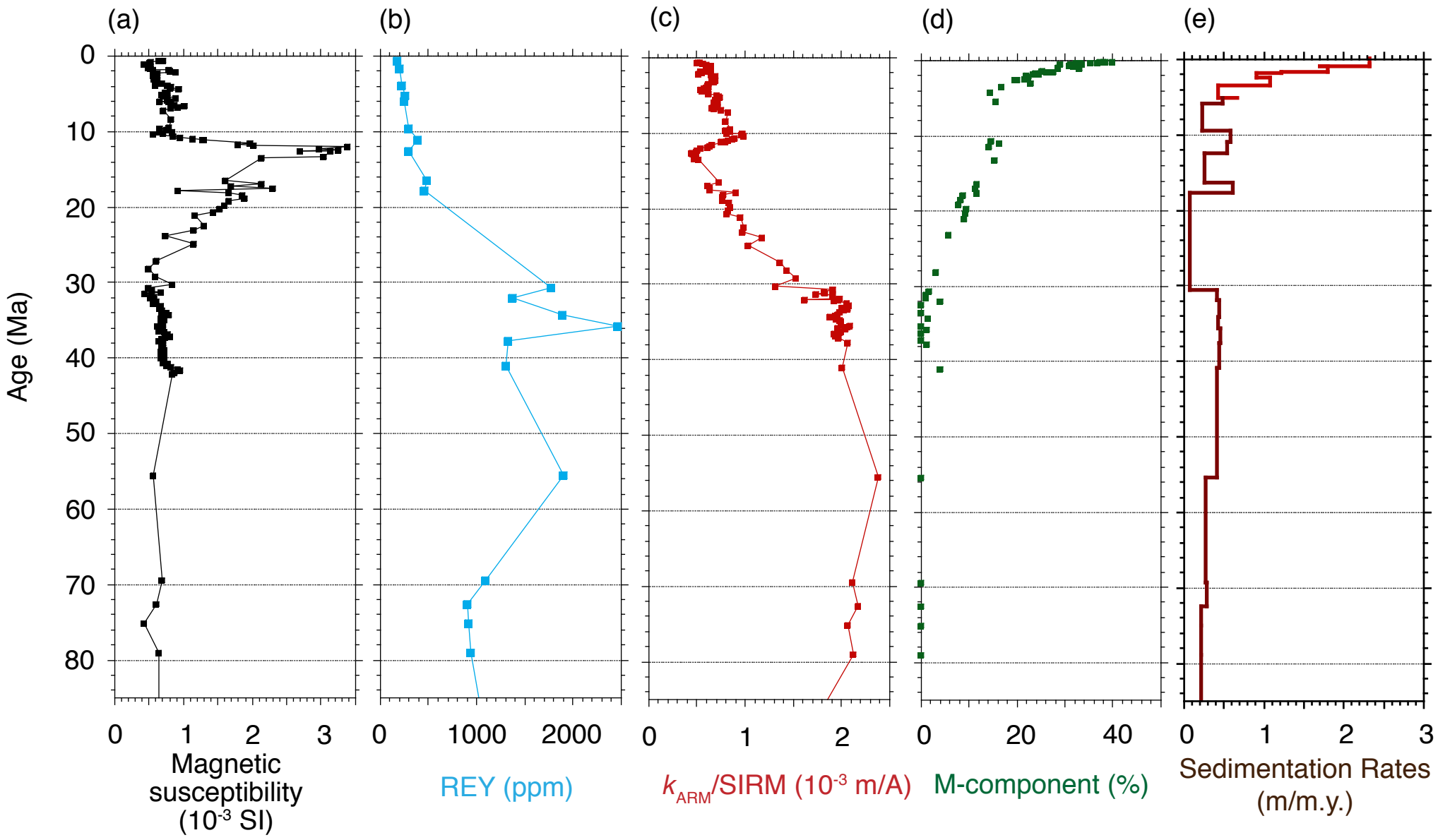
(a)
(b)
(c)
(d)
(e)
Age (Ma)
0
10
20
30
40
50
60
70
80
0
1
2
3
Magnetic susceptibility (10^{-3} SI)
0
1000
2000
REY (ppm)
0
1
2
k_{ARM}/SIRM (10^{-3} m/A)
0
20
40
M-component (%)
0
1
2
3
Sedimentation Rates (m/m.y.)

Figure 5-2

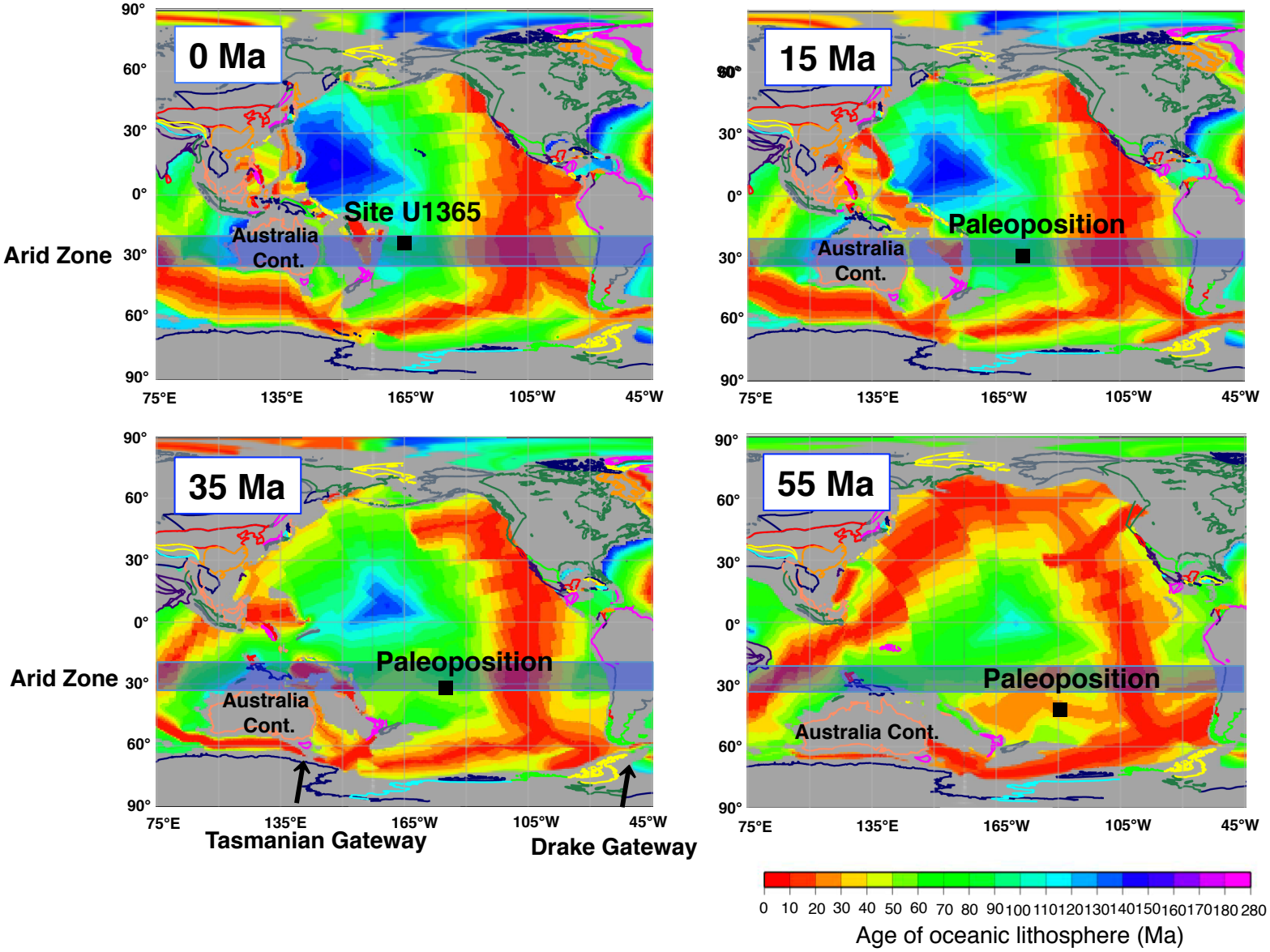
0 Ma
Site U1365
Australia Cont.
Arid Zone
15 Ma
Paleoposition
Australia Cont.
35 Ma
Paleoposition
Australia Cont.
Arid Zone
Tasmanian Gateway
Drake Gateway
55 Ma
Paleoposition
Australia Cont.
90°
60°
30°
0°
30°
60°
90°
75°E
135°E
165°W
105°W
45°W
0 10 20 30 40 50 60 70 80 90 100 110 120 130 140 150 160 170 180 280
Age of oceanic lithosphere (Ma)

Figure 5-3

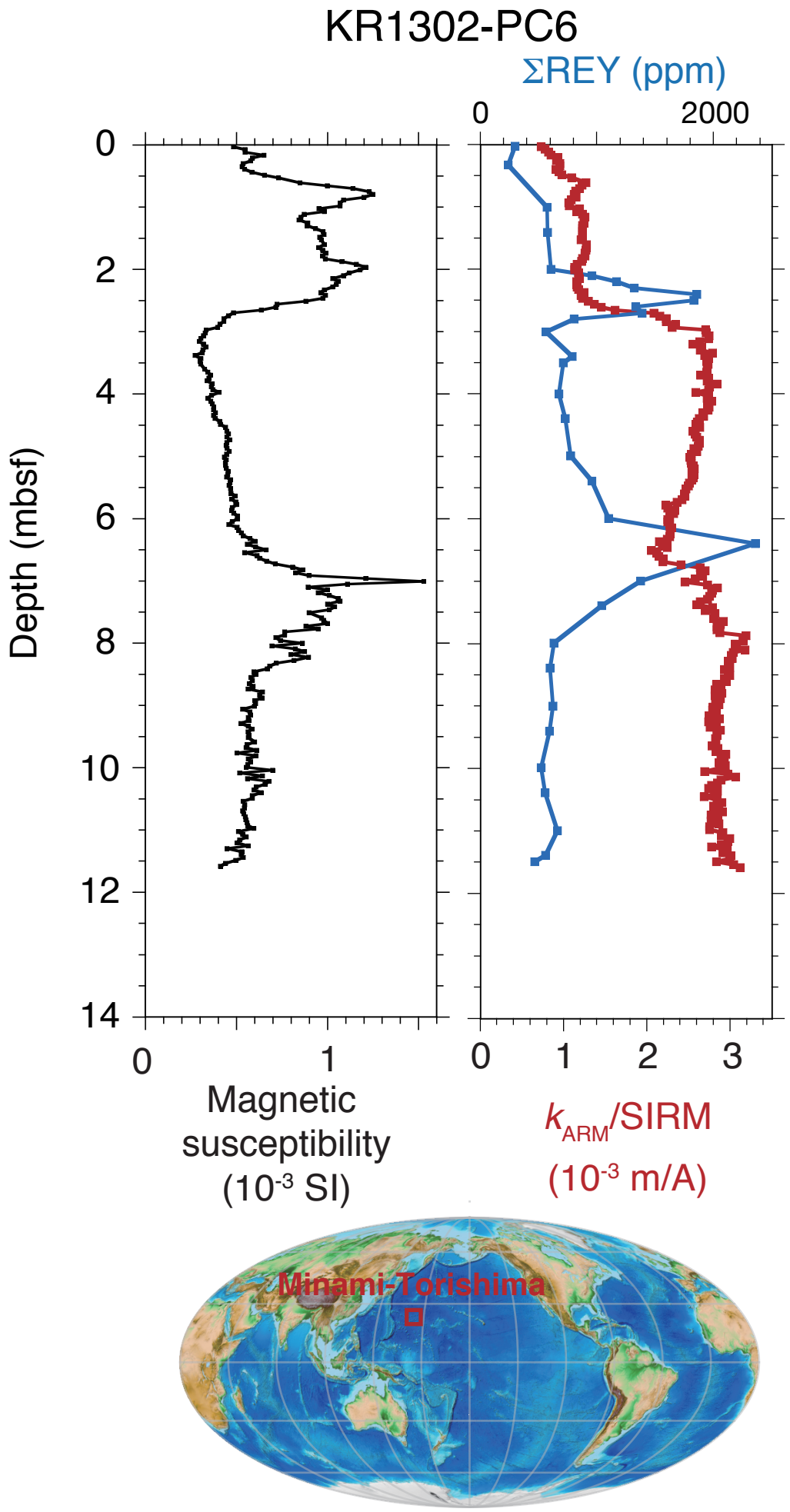
KR1302-PC6
ΣREY (ppm)
0
2000
Depth (mbsf)
0
2
4
6
8
10
12
14
0
1
Magnetic susceptibility (10^{-3} SI)
0
1
2
3
k_{ARM}/SIRM (10^{-3} m/A)
Minami-Torishima

Figure 5-4